Second-harmonic generation frequency-resolved optical gating in the single-cycle regime

Baltuška, Andrius; Pshenichnikov, Maxim S.; Wiersma, Douwe A.

Published in:
IEEE Journal of Quantum Electronics

IMPORTANT NOTE: You are advised to consult the publisher's version (publisher's PDF) if you wish to cite from it. Please check the document version below.

Document Version
Publisher's PDF, also known as Version of record

Publication date:
1999

Link to publication in University of Groningen/UMCG research database

Citation for published version (APA):
Baltuška, A., Pshenichnikov, M. S., & Wiersma, D. A. (1999). Second-harmonic generation frequency-resolved optical gating in the single-cycle regime. *IEEE Journal of Quantum Electronics*, *35*(4), 459 - 478.

Second-Harmonic Generation Frequency-Resolved Optical Gating in the Single-Cycle Regime

Andrius Baltuška, Maxim S. Pshenichnikov, and Douwe A. Wiersma

(Invited Paper)

Abstract—The problem of measuring broad-band femtosecond pulses by the technique of second-harmonic generation frequency-resolved optical gating (SHG FROG) is addressed. We derive the full equation for the FROG signal, which is valid even for single-optical-cycle pulses. The effect of the phase mismatch in the second-harmonic crystal, the implications of the beam geometry, and the frequency-dependent variation of the nonlinearity are discussed in detail. Our numerical simulations show that, under carefully chosen experimental conditions and with a proper spectral correction of the data, the traditional FROG inversion routines work well even in the single-cycle regime. The developed description of the SHG FROG signal was applied to measure the white-light continuum pulses in the spectral region of 500–1100 nm. The obtained spectral phase of these pulses served as a target function for the pulse compressor design. The pulses produced by compression around 800 nm were also characterized by SHG FROG. The resulting pulse duration measures 4.5 fs which corresponds to ∼2.5 optical cycles.

Index Terms—Frequency conversion, nonlinear optics, optical beam focusing, optical pulse compression, optical pulse measurements, ultrafast optics.

I. INTRODUCTION

RECENT progress in complete characterization of ultrashort pulses reflects the growing demand for detailed information on pulse structure and phase distortion. This knowledge plays a decisive role in the outcome of many applications. For instance, it has been recognized that pulses with identical spectra but different spectral phases can strongly enhance efficiency of high-harmonic generation [1], affect wavepacket motion in organic molecules [2], [3], enhance population inversion in liquid [4] and gas [5] phases, and even steer a chemical reaction in a predetermined direction [6]. Moreover, a totally automated search for the best pulse was recently demonstrated to optimize a preselected reaction channel [7]. Then, by measuring the phase and amplitude of the excitation pulses, one can perform a back-reconstruction of potential surfaces of the parent molecule.

The complete determination of the electric field of femtosecond pulses also uncovers the physics behind their generation as

has been demonstrated in the case of femtosecond Ti:sapphire lasers [8], [9]. Such information is invaluable to determine the ways of and ultimate limits for further pulse shortening. Last, owing to the great complexity of broad-band phase correction required to produce spectrum-limited pulses with durations shorter than 5 fs [10]–[13], the characterization of the white-light continuum as well as compressed pulses becomes mandatory.

A breakthrough in the full characterization of ultrashort pulses occurred five years ago with the introduction of frequency-resolved optical gating (FROG) [14], [15]. FROG measures a two-dimensional (2-D) spectrogram in which the signal of any autocorrelation-type experiment is resolved as a function of both time delay and frequency. The full pulse intensity and phase may be subsequently retrieved from such a spectrogram (called FROG trace) via an iterative retrieval algorithm. Notably, no *a priori* information about the pulse shape, as it is always the case for conventional autocorrelation measurements, is necessary to reconstruct the pulse from the experimental FROG trace.

In general, FROG is quite accurate and rigorous [16]. Because a FROG trace is a plot of both frequency and delay, the likelihood of the same FROG trace corresponding to different pulses is very low. Additionally, the great number of data points in the 2-D FROG trace makes it under equivalent conditions much less sensitive to noise than the pulse diagnostics based on one-dimensional (1-D) measurements, such as the ordinary autocorrelation. Last but not least, FROG offers self-consistency checks for data that are unavailable in other pulse-measuring techniques. This feedback mechanism involves computing the temporal and spectral marginals that are the integrals of the FROG trace along the delay and frequency axes. The comparison of the marginals with the independently measured fundamental spectrum and autocorrelation verifies the validity of the measured FROG trace [9], [17], [18]. To date, FROG methods have been applied to measure a vast variety of pulses with different duration, wavelength, and complexity [19].

A number of outstanding features make FROG especially valuable for the measurement of extremely short pulses in the range of 10 fs and below.

First, since FROG utilizes the excite–probe geometry, common for most nonlinear optical experiments, it is ideally suited to characterize pulses that are used in many spectroscopic laboratories. Unlike other pulse diagnostics [20]–[24], FROG does

not require splitting of auxiliary laser beams and prefabrication of reference pulses. This fact is of great practical relevance, since the setup complexity in many spectroscopic experiments is already quite high [25]–[31]. Therefore, it is desirable to minimize the additional effort and setup modifications that are necessary for proper pulse diagnostics. FROG directly offers this possibility. Pulse characterization is performed precisely at the position of the sample by simply interchanging the sample with a nonlinear medium for optical gating. The last point becomes especially essential for the pulses consisting of only several optical cycles [10]–[13], [32] currently available for spectroscopy. The dispersive lengthening that such pulses experience even due to propagation through air precludes the use of a separate diagnostics device. Thus, FROG is the ideal way to measure and optimize pulses on target prior to carrying out a spectroscopic experiment.

Second, it is still possible to correctly measure such short pulses by FROG even in the presence of systematic errors. Several types of such errors will inevitably appear in the measurement of pulses whose spectra span over a hundred nanometers or more. For example, a FROG trace affected by wavelength-dependent detector sensitivity and frequency conversion efficiency can be validated via the consistency checks [9]. In contrast, an autocorrelation trace measured under identical conditions may be corrupted irreparably.

Third, the temporal resolution of the FROG measurement is not limited by the sampling increment in the time domain, provided the whole time–frequency spectrogram of the pulse is properly contained within the measured FROG trace. The broadest feature in the frequency domain determines in this case the shortest feature in the time domain. Therefore, no fine pulse structure can be overlooked [19], even if the delay increment used to collect the FROG trace is larger than the duration of such a structure. Thus, reliability of the FROG data relies more on the proper delay axis calibration rather than on the very fine sampling in time, which might be troublesome considering that the pulse itself measures only a couple of micrometers in space.

Choosing the appropriate type of autocorrelation that can be used in FROG (so-called FROG geometries [17], [19]), one must carefully consider possible distortions that are due to the beam arrangement and the nonlinear medium. Consequently, not every FROG geometry can be straightforwardly applied to measure extremely short pulses, i.e., 10 fs and below. In particular, it has been shown that in some $\chi^{\langle 3 \rangle}$-based techniques (for instance, polarization-gating, transient grating, etc.) the finite response time due to the Raman contribution to nonlinearity played a significant role even in the measurement of 20-fs pulses [33]. Therefore, the FROG with the use of the second-harmonic generation (SHG) in transparent crystals [34]–[36] and surface third-harmonic generation [37], that have instantaneous nonlinearity, presents the best choice for the measurement of the shortest pulses available to date.

Another important experimental concern is the level of the signal to be detected in the FROG measurement. Among different FROG variations, its version based on SHG is the most appropriate technique for low-energy pulses. Obviously,

SHG FROG [34] potentially has a higher sensitivity than the FROG geometries based on third-order nonlinearities that under similar circumstances are much weaker. Different spectral ranges and polarizations of the SHG FROG signal and the fundamental radiation allow the effective suppression of the background, adding to the suppression provided by the geometry. The low-order nonlinearity involved, combined with the background elimination, results in the higher dynamic range in SHG FROG than in any other FROG geometry.

In general, the FROG pulse reconstruction does not depend on pulse duration since the FROG traces simply scale in the time–frequency domain. However, with the decrease of the pulse duration that is accompanied by the growth of the bandwidth, the experimentally collected data begin to deviate significantly from the mathematically defined ideal FROG trace. Previous studies [8], [9] have addressed the effect of the limited phase-matching bandwidth of the nonlinear medium [38] and time smearing due to noncollinear geometry on SHG FROG measurement which become increasingly important for 10-fs pulses. The possible breakdown of the slowly-varying envelope approximation and frequency dependence of the nonlinearity are the other points of concern for the pulses that consist of a few optical cycles. Some of these issues have been briefly considered in our recent letter [39].

In this paper, we provide a detailed description of SHG FROG performance for ultrabroad-band pulses, the bandwidths of which correspond to 3-fs spectral-transformed duration. Starting from the Maxwell equations, we derive a complete expression for the SHG FROG signal that is valid even in a single-cycle pulse regime and includes phase matching in the crystal, beam geometry, dispersive pulse-broadening inside the crystal, and dispersion of the second-order nonlinearity. Subsequently, we obtain a simplified expression that decomposes the SHG FROG signal to a product of the ideal SHG FROG and a spectral filter applied to the second-harmonic (SH) radiation. Numerical simulations, presented later in the paper, convincingly show that the approximations made upon the derivation of the simplified expression are well justified. Finally, we demonstrate practical applications of SHG FROG technique to strongly chirped ultrabroad-band pulses and compressed 4.5-fs pulses.

The outline of this paper follows. In Section II, we define the pulse intensity and phase in time and frequency domains. In Section III, the spatial profile of ultrabroad-band pulses is addressed. The complete expression for SHG FROG signal for single-cycled pulses is derived in Section IV. We discuss the ultimate time resolution of the SHG FROG in Section V. The approximate expression for the SHG FROG signal obtained in Section VI is verified by numerical simulations in Section VII. In Section VIII, we briefly comment on Type II phase matching in SHG FROG measurements. Section IX provides several useful pieces of advise on the choice of the SHG crystal. Possible distortions of the experimental data resulting from spatial filtering are considered in Section X. In Section XI we describe our SHG FROG apparatus. SHG FROG characterization of the white-light continuum and 4.5-fs pulses is demonstrated in Sections XII and XIII, respectively. Finally, in Section XIV, we summarize our findings.

II. AMPLITUDE AND PHASE CHARACTERIZATION OF THE PULSE

The objective of a FROG experiment lies in finding the pulse intensity and phase in time, that is $I(t)$, $\varphi(t)$ or, equivalently, in frequency $\tilde{I}(\omega)$, $\tilde{\varphi}(\omega)$. The laser pulse is conventionally defined by its electric field

$$E(t) = A(t) \exp(i\varphi(t)) \qquad (1)$$

where $A(t)$ is the modulus of the time-dependent amplitude and $\varphi(t)$ is the time-dependent phase. The temporal pulse intensity $I(t)$ is determined as $I(t) \propto A^2(t)$. The time-dependent phase contains information about the change of instantaneous frequency as a function of time (the so-called chirp) that is given by [40], [41]

$$\omega(t) = \frac{\partial \varphi(t)}{\partial t}. \qquad (2)$$

The chirped pulse, therefore, experiences a frequency sweep in time, i.e., changes frequency within the pulse length.

The frequency-domain equivalent of pulse field description is

$$\tilde{E}(\omega) = \int E(t) \exp(i\omega t)\, dt \equiv \tilde{A}(\omega) \exp(i\tilde{\varphi}(\omega)) \qquad (3)$$

where $\tilde{E}(\omega)$ is the Fourier transform of $E(t)$ and $\tilde{\varphi}(\omega)$ is the frequency-dependent (or spectral) phase. Analogously to the time domain, the spectral intensity, or the pulse spectrum, is defined as $\tilde{I}(\omega) \propto \tilde{A}^2(\omega)$. The relative time separation among various frequency components of the pulse, or group delay, can be determined by [41]

$$\tau(\omega) = \frac{\partial \tilde{\varphi}(\omega)}{\partial \omega}. \qquad (4)$$

Hence, the pulse with a flat spectral phase is completely "focused" in time and has the shortest duration attainable for its bandwidth.

It is important to notice that none of the presently existing pulse-measuring techniques retrieve the absolute phase of the pulse, i.e., pulses with phases $\varphi(t)$ and $\varphi(t) + \varphi_0$ appear to be identical [42]. Indeed, all nonlinear processes employed in FROG are not sensitive to the absolute phase. However, the knowledge of this phase becomes essential in the strong-field optics of nearly single-cycled pulses [43], [44]. It has been suggested [45] that the absolute phase may be assessable via photo-emission in the optically tunneling regime [46].

In fact, the full pulse characterization remains incomplete without the analysis of spatio-temporal or spatio-spectral distribution of the pulse intensity. In this paper, we assume that the light field is linearly polarized and that each spectral component of it has a Gaussian spatial profile. The Gaussian beam approximation is discussed in detail in Section III.

III. PROPAGATION AND FOCUSING OF SINGLE-CYCLE PULSES

The spatial representation of a pulse of which its spectral width is close to its carrier frequency is a nontrivial problem. Because of diffraction, lower frequency components have stronger divergence compared with high-frequency ones. As a consequence, such pulse parameters as the spectrum and duration are no longer constants and may change appreciably as the beam propagates even in free space [47].

We represent a Gaussian beam field in the focal plane as

$$\tilde{\mathsf{E}}(x,y,\omega) = \tilde{E}(\omega)\sqrt{\frac{2\ln 2}{\pi}}\frac{1}{d(\omega)}\exp\left[-2\ln 2\frac{x^2+y^2}{d^2(\omega)}\right] \qquad (5)$$

where $d(\omega)$ is the beam diameter (FWHM) of the spectral component with the frequency ω and x and y are transverse coordinates. The normalization terms are chosen to provide the correct spectrum integrated over the beam as measured by a spectrometer

$$\tilde{I}(\omega) \propto \iint |\tilde{\mathsf{E}}(x,y,\omega)|^2\, dx\, dy. \qquad (6)$$

We now calculate the beam diameter after propagating a distance z

$$d(\omega, z) = d(\omega, z=0)\sqrt{1 + \left(\frac{2cz}{d^2(\omega, z=0)\omega}\right)^2} \qquad (7)$$

where c is the speed of light in vacuum. To avoid the aforementioned problems, we require diameters of different spectral components to scale proportionally as the Gaussian beam propagates in free space, i.e.,

$$d^2(\omega, z=0)\omega = \text{const.} \qquad (8)$$

The constant in (8) can be defined by introducing the FWHM beam diameter d_0 at the central frequency ω_0. Therefore, the electric field of the Gaussian beam given by (5) becomes

$$\tilde{\mathsf{E}}(x,y,\omega) = \tilde{E}(\omega)\sqrt{\frac{2\ln 2}{\pi}}\frac{1}{d_0}\sqrt{\frac{\omega}{\omega_0}}\exp\left[-2\ln 2\frac{x^2+y^2}{d_0^2}\frac{\omega}{\omega_0}\right]. \qquad (9)$$

At this point, the question can be raised about the low-frequency components, the size of which, according to (9), becomes infinitely large. However, the spectral amplitude of these components decreases rapidly with frequency. For instance, the spectral amplitude of a single-cycle Gaussian pulse with a central frequency ω_0 is given by

$$\tilde{A}(\omega) = \exp\left[-\frac{\pi^2}{2\ln 2}\left(1 - \frac{\omega}{\omega_0}\right)^2\right]. \qquad (10)$$

Consequently, the amplitude of the electric field at zero frequency amounts to only 0.1% of its peak value.

The spatial frequency distribution was observed experimentally with focused terahertz beams [48] and was discussed recently by Feng *et al.* [49]. Note that our definition of transversal spectral distribution in the beam implies that confocal parameters of all spectral components are identical

$$b = \frac{d^2(\omega, z=0)\omega}{4\ln 2} = \frac{d_0^2\omega_0}{4\ln 2}. \qquad (11)$$

This is totally consistent with the beam size in laser resonators where longer wavelength components have a larger beam size. The spatial distribution of radiation produced due to self-phase modulation in single-mode fibers is more complicated. First, the transverse mode is described by the zeroth-order Bessel
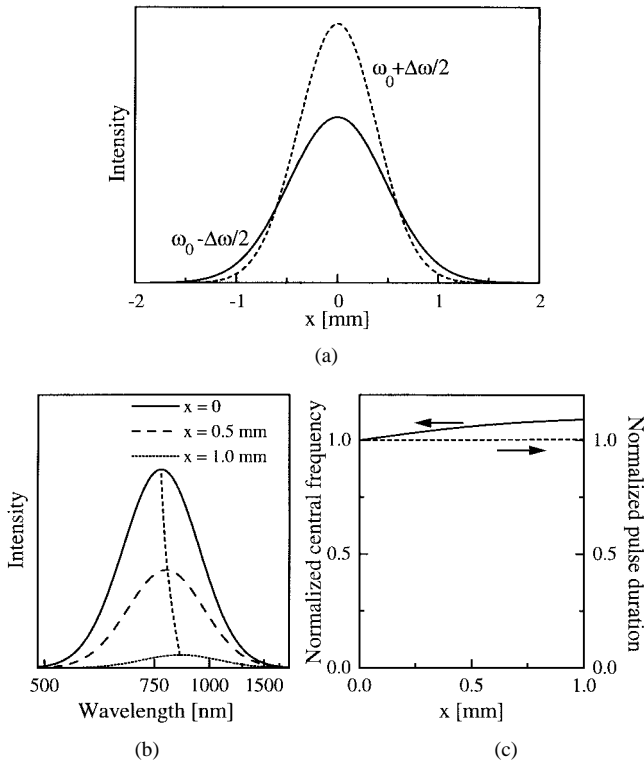
Fig. 1. Spatial parameters of an ideal single-cycle Gaussian pulse centered at 800 nm. (a) Spatial intensity profiles of two spectral components that are separated by FWHM $\Delta\omega$ from the central frequency ω_0. (b) Intensity spectra as a function of transverse coordinate x. (c) Dependence of pulse central frequency (solid curve) and pulse duration (dashed curve) on transverse coordinate x. The beam axis corresponds to $x = 0$.

function [50]. Second, near the cut-off frequency, the mode diameter experiences strong changes [51]. However, for short pieces of fiber conventionally used for pulse compression and reasonable values of a normalizad frequency V [50], it can be shown that a Gaussian distrubution given by (9) is an acceptable approximation. The situation with hollow waveguides [52] is quite different since all spectral components have identical radia [53].

Another important issue concernes beam focusing, which should not change the distribution of spectral components. Since the equations for mode matching contain only confocal parameters [54], the validity of (9) at the new focal point is automatically fulfilled provided, of course, the focusing remains achromatic.

Although (9) ensures that different spectral components scale identically during beam propagation and focusing, it also implies that the pulse spectrum changes along the transversal coordinates. Fortunately, this effect is negligibly small even in the single-cycle regime. Fig. 1(a) shows the spatial intensity distribution of several spectral components of a Gaussian single-cycle pulse with a central wavelength of 800 nm. As one moves away from the beam axis, a red shift is clearly observed [Fig. 1(b)], since the higher frequency spectral components are contained in tighter spatial modes. However, the change of the carrier frequency does not exceed 10% (Fig. 1(c), solid line), while the variation of the pulsewidth is virtually undetectable (Fig. 1(c), dotted line). Therefore, this kind of spatial chirp can be disregarded even for the shortest optical pulses.
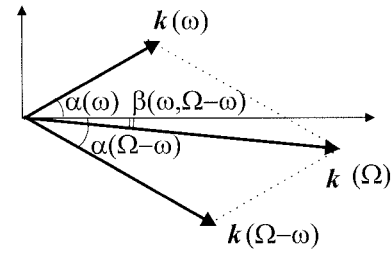

Fig. 2. Noncollinear phase matching for three-wave interaction. $\mathbf{k}(\omega)$ and $\mathbf{k}(\Omega - \omega)$ are the wavevectors of the fundamental fields that form an angle α with the z axis. $\mathbf{k}_{\mathrm{SH}}(\Omega)$ is the wavevector of the SH that intersects the z axis at an angle β.

IV. THE SHG FROG SIGNAL IN THE SINGLE-CYCLE REGIME

In this section, the complete equation that describes the SHG FROG signal for pulses as short as one optical cycle is derived. We consistently include such effects as phase-matching conditions in a nonlinear crystal, time-smearing effects due to noncollinear geometry, spectral filtering of the SH radiation, and dispersion of the second-order nonlinearity.

We consider the case of noncollinear geometry in which the fundamental beams intersect at a small angle (Fig. 2). As it has been pointed out [38], pulse broadening due to crystal bulk dispersion is negligibly small compared to the group-velocity mismatch. This means that the appropriate crystal thickness should mostly be determined from the phase-matching conditions. For instance, in a 10-μm BBO crystal, the bulk dispersion broadens a single-cycle pulse by only $\sim$0.1 fs while the group-velocity mismatch between the fundamental and SH pulses is as much as 0.9 fs.

We assume such focusing conditions of the fundamental beams that the confocal parameter and the longitudinal beam overlap of the fundamental beams are considerably longer than the crystal length. For instance, for an ideal Gaussian beam of $\sim$2-mm diameter focused by a 10-cm achromatic lens, the confocal parameter, that is, the longitudinal extent of the focal region, is $\sim$1.2 mm. This is considerably longer than the practical length of the nonlinear crystal. Under such conditions, wavefronts of the fundamental waves inside the crystal are practically flat. Therefore, we treat the SHG as a function of the longitudinal coordinate only and include the transversal coordinates at the last step to account for the spatial beam profile [see (9)]. Note that the constraint on the focusing is not always automatically fulfilled. For example, the use of a 1-cm lens in the situation described above reduces the length of the focal region to only 12 μm, and, in this case, it is impossible to disregard the dependence on transverse coordinates.

We assume that the SH field is not absorbed in the nonlinear crystal. This is well justified even for single-cycle pulses. Absorption bands of the crystals that are transparent in the visible start at $\sim$200 nm. Consequently, at these frequencies the field amplitude decreases by a factor $\exp(-\pi^2/2\ln 2) \approx 0.001$ [see (10)] compared to its maximum at 400 nm. We also require the efficiency of SHG to be low enough to avoid depletion of the fundamental beams. Hence, the system of two coupled equations describing nonlinear interaction [55] is

reduced to one. The equation that governs propagation of the SH wave in the $+z$ direction inside the crystal can be obtained directly from Maxwell's equations [56]

$$\frac{\partial^2}{\partial z^2}E_{SH}(z,t) - \varepsilon_0\mu_0\frac{\partial^2}{\partial t^2}\int_{-\infty}^{t}\varepsilon(t-t')E_{SH}(z,t')\,dt'$$
$$= \mu_0\frac{\partial^2}{\partial t^2}P^{\langle 2\rangle}(z,t) \quad (12)$$

where $E_{SH}(z,t)$ is the SH field, $\mu_0\varepsilon_0 = 1/c^2$, ε is the relative permittivity, and $P^{\langle 2\rangle}(z,t)$ is the induced second-order dielectric polarization. By writing both $E_{SH}(z,t)$ and $P^{\langle 2\rangle}(z,t)$ as a Fourier superposition of monochromatic waves, one obtains a simple equivalent of (12) in the frequency domain

$$\frac{\partial^2}{\partial z^2}\tilde{E}_{SH}(z,\Omega) + k_{SH}^2(\Omega)\tilde{E}_{SH}(z,\Omega) = -\mu_0\Omega^2\tilde{P}^{\langle 2\rangle}(z,\Omega)$$
$$(13)$$

where $\tilde{E}_{SH}(z,\Omega)$ and $\tilde{P}^{\langle 2\rangle}(z,\Omega)$ are Fourier transforms of $E_{SH}(z,t)$ and $P^{\langle 2\rangle}(z,t)$, respectively, Ω is the frequency, and $k_{SH}(\Omega)$ is the wavevector of the second harmonic field: $k_{SH}^2(\Omega) = \Omega^2\varepsilon_0\mu_0\tilde{\varepsilon}(\Omega)$, with $\tilde{\varepsilon}(\Omega)$ being the Fourier transform of the relative permittivity $\varepsilon(t)$.

In order to simplify the left part of (13), we write the SH field as a plane wave propagating along the z axis

$$\tilde{E}_{SH}(z,\Omega) = \tilde{\mathcal{E}}_{SH}(z,\Omega)\exp(ik_{SH}(\Omega)z) \quad (14)$$

whence (13) becomes

$$2ik_{SH}(\Omega)\frac{\partial}{\partial z}\tilde{\mathcal{E}}_{SH}(z,\Omega) + \frac{\partial^2}{\partial z^2}\tilde{\mathcal{E}}_{SH}(z,\Omega)$$
$$= -\mu_0\Omega^2\tilde{P}^{\langle 2\rangle}(z,\Omega)\exp(-ik_{SH}(\Omega)z). \quad (15)$$

So far, we have made no simplifications concerning the pulse duration. Now we apply the slowly-varying amplitude approximation [56], i.e.,

$$\left|\frac{\partial}{\partial z}\tilde{\mathcal{E}}_{SH}(z,\Omega)\right| \ll |2k_{SH}(\Omega)\tilde{\mathcal{E}}_{SH}(z,\Omega)| \quad (16)$$

in order to omit the term $\frac{\partial^2}{\partial z^2}\tilde{\mathcal{E}}_{SH}(z,\Omega)$. Nonequality (16) is a good approximation even for single-cycle pulses propagating in transparent media [57]. The only point of concern is related to the lowest frequencies for which k_{SH} becomes close to zero. However, as we have already mentioned in Section III, the amplitude of such components do not exceed 0.1% of the maximum and therefore can be disregarded. Consequently, (15) can be readily solved by integration over the crystal length L

$$\tilde{\mathcal{E}}_{SH}(L,\Omega) = i\frac{c\mu_0\Omega}{2n_{SH}(\Omega)}\int_0^L\tilde{P}^{\langle 2\rangle}(z,\Omega)\exp(-k_{SH}(\Omega)z)\,dz$$
$$(17)$$

where $n_{SH}(\Omega) = \sqrt{\tilde{\varepsilon}(\Omega)}$ is the refractive index for the SH wave. Now we should calculate the second-order polarization $\tilde{P}^{\langle 2\rangle}(z,\Omega)$. We assume that two fundamental fields cross in the xz plane at a small angle $2\alpha_0$ (see Fig. 2). The inclination with the z axis of each beam inside the crystal is then $\alpha(\omega) = \arcsin[n(\omega)\sin\alpha_0] \approx \alpha_0 n(\omega)$. We denote the relative

delay between the pulses as τ. An additional delay for off-axis components of the beam due to the geometry can be expressed for a plane wave as $\tau'(x) = xn(\omega)\sin\alpha(\omega)/c = x\sin\alpha_0/c \approx x\alpha_0/c$ for the beam propagating in $+\alpha$ direction, and $\tau'(x) \approx -x\alpha_0/c$ for the beam in the $-\alpha$ direction. The electric fields in the frequency domain can be found via Fourier transforms

$$\tilde{E}_1(\omega) = \tilde{E}(\omega)\exp(i\omega(x\alpha_0/c))$$
$$\tilde{E}_2(\omega) = \tilde{E}(\omega)\exp(i\omega(-x\alpha_0/c - \tau)). \quad (18)$$

In order to calculate the second-order dielectric polarization induced at frequency Ω by the two fundamental fields, we should sum over all possible permutations of fundamental frequencies

$$\tilde{P}^{\langle 2\rangle}(z,\Omega) = \int\tilde{\chi}^{\langle 2\rangle}(\Omega,\omega,\Omega-\omega)\tilde{E}_1(\omega)\tilde{E}_2(\Omega-\omega)\,d\omega$$
$$= \exp(i\Omega(\tau + x\alpha_0/c))\int\tilde{\chi}^{\langle 2\rangle}(\Omega,\omega,\Omega-\omega)$$
$$\times\tilde{\mathcal{E}}(\omega)\tilde{\mathcal{E}}(\Omega-\omega)\exp[i(k_z(\omega)z + k_z(\Omega-\omega)z$$
$$+ \omega(\tau + 2x\alpha_0/c))]\,d\omega. \quad (19)$$

In (19), we included frequency dependence of the nonlinear susceptibility $\tilde{\chi}^{\langle 2\rangle}(\Omega,\omega,\Omega-\omega)$ and represent the fundamental fields analogously to (14). The electric field of the SH therefore becomes

$$\tilde{\mathcal{E}}_{SH}(L,\Omega)$$
$$= i\frac{c\mu_0\Omega L}{2n(\Omega)}\exp(i\Omega(\tau + x\alpha_0/c))\int\tilde{\chi}^{\langle 2\rangle}(\Omega,\omega,\Omega-\omega)$$
$$\times\tilde{\mathcal{E}}(\Omega-\omega)\tilde{\mathcal{E}}(\omega)\exp\left(i\frac{\Delta k(\omega,\Omega-\omega)L}{2}\right.$$
$$\left.+ i\omega\left(\tau + \frac{2x\alpha_0}{c}\right)\right)\text{sinc}\left(\frac{\Delta k(\omega,\Omega-\omega)L}{2}\right)d\omega \quad (20)$$

where $\Delta k(\omega,\Omega-\omega)$ is the phase mismatch given by the equation

$$\Delta k(\omega,\Omega-\omega) = k(\omega)\cos(\alpha_0 n_1(\omega))$$
$$+ k(\Omega-\omega)\cos(\alpha_0 n_2(\Omega-\omega))$$
$$- k_{SH}(\Omega)\cos\beta(\omega,\Omega-\omega) \quad (21)$$

with n_1 and n_2 the refractive indices of the fundamental waves and $\beta(\omega,\Omega-\omega)$ the angle between $\mathbf{k}_{SH}(\Omega)$ and the z axis inside the crystal. The appearance of this angle can be easily understood from Fig. 2. The momentum conservation law determines the direction of the emitted SH field

$$\mathbf{k}(\omega) + \mathbf{k}(\Omega-\omega) = \mathbf{k}_{SH}(\Omega) \quad (22)$$

where $\mathbf{k}(\omega)$ and $\mathbf{k}(\Omega-\omega)$ are the wavevectors of the incident fundamental waves. In the case $k(\omega) \neq k(\Omega-\omega)$, β is nonzero and it can be found from the following equation[1]:

$$\sin\beta(\omega,\Omega-\omega) = \sin\alpha_0\frac{k(\omega)n_1(\omega) - k(\Omega-\omega)n_2(\Omega-\omega)}{k_{SH}(\Omega)}.$$
$$(23)$$

---

[1] In fact, if the SH is an extraordinary wave, the magnitude of $k_{SH}(\Omega)$ in (23) is a function of $\beta(\omega,\Omega-\omega)$. The problem of finding the exact values of both $k_{SH}(\Omega)$ and $\beta(\omega,\Omega-\omega)$ could be easily solved by employing the relations of crystaloptics and (23). However, (23) alone gives an excellent approximation for $\beta(\omega,\Omega-\omega)$ if one chooses $k_{SH}(\Omega)|_{\beta=0}$.

Since β is the same order of magnitude as the intersection angle, the correction $\cos\beta(\omega,\Omega-\omega)$ is required only in the Δk expression [see (21)]. Elsewhere this correction can be dropped.

The values of the wavevectors and refractive indices in (21) and (23) depend on the actual polarization of the three interacting waves. Thus, for Type I phase matching, we obtain

$$
\begin{aligned}
\Delta k(\omega,\Omega-\omega) &= k_O(\omega)\cos(\alpha_0 n_O(\omega)) \\
&\quad + k_O(\Omega-\omega)\cos(\alpha_0 n_O(\Omega-\omega)) \\
&\quad - k_E(\Omega)\cos\beta(\omega,\Omega-\omega)
\end{aligned}
\tag{24}
$$

and for Type II

$$
\begin{aligned}
\Delta k(\omega,\Omega-\omega) &= k_E(\omega)\cos(\alpha_0 n_E(\omega)) \\
&\quad + k_O(\Omega-\omega)\cos(\alpha_0 n_O(\Omega-\omega)) \\
&\quad - k_E(\Omega)\cos\beta(\omega,\Omega-\omega).
\end{aligned}
\tag{25}
$$

Here indices O and E correspond to the ordinary and extraordinary waves, respectively.

To calculate the total FROG signal, one should integrate the signal intensity

$$
\tilde{I}_{\mathrm{SH}}(L,\Omega) = \varepsilon_0 \frac{n_{\mathrm{SH}}(\Omega)}{c} |\tilde{\mathcal{E}}_{\mathrm{SH}}(L,\Omega)|^2
\tag{26}
$$

over the transverse coordinates x and y. Hence, for the SH signal detected in FROG, we obtain

$$
\begin{aligned}
&S(\Omega,\tau,L) \\
&= \frac{\Omega^2 L^2 \sqrt{\Omega} Q(\Omega)}{2c^3 \varepsilon_0 n_{\mathrm{SH}}(\Omega)} \left[\frac{\ln 2}{\pi\omega_0}\right]^{3/2} \int \exp\left(-4\ln 2\left(\frac{x}{d_0}\right)^2 \frac{\Omega}{\omega_0}\right) \\
&\quad \times \left| \int \tilde{\chi}^{\langle 2 \rangle}(\Omega,\omega,\Omega-\omega)\sqrt{\omega\left(1-\frac{\omega}{\Omega}\right)} \right. \\
&\quad \times \tilde{\mathcal{E}}(\Omega-\omega)\tilde{\mathcal{E}}(\omega)\exp\left(i\frac{\Delta k(\omega,\Omega-\omega)L}{2}\right. \\
&\quad \left.\left. + i\omega\left(\tau+\frac{2x\alpha_0}{c}\right)\right)\mathrm{sinc}\left(\frac{\Delta k(\omega,\Omega-\omega)L}{2}\right)d\omega\right|^2 dx.
\end{aligned}
\tag{27}
$$

In (27), $Q(\Omega)$ is the spectral sensitivity of the photodetector. We also took into consideration the transverse profiles of the fundamental beams as given in Section III.

Thus far, we have limited our discussion to the case of low-efficiency SHG, i.e., when the depletion of the fundamental waves can be disregarded. In the high conversion efficiency regime, however, additional effects play an important role. While the SH intensity depends quadratically on the crystal length L in the case of an undepleted pump [58], in the high-efficiency regime, conversion efficiency "saturates" for more intense spectral modes but remains proportional to L^2 for the weaker ones. Consequently, the FROG traces measured in a Type I SHG crystal in the presence of significant pump depletion typically have both spectral and temporal marginals broader than those in the low-conversion-efficiency case. Hence, despite seemingly increased bandwidth in the high-efficiency regime, the FROG trace is intrinsically incorrect. The case of the high-efficiency SHG in a Type II crystal [59], [60] is more complex than in Type I and can

result in both shortening and widening of the temporal width of the FROG trace. Another important example of the SH spectral shaping in the high-conversion-efficiency regime is the nonlinear absorption of the frequency-doubled radiation inside the SHG crystal [61]. Therefore, the high-efficiency SH conversion is a potential source of systematic errors in a FROG experiment and should be avoided.

To conclude this section, we would like to make a remark on the frequency—as opposed to time—domain approach to the wave equation (12) in the single-optical-cycle regime. Clearly, the former has a number of advantages. The spectral amplitude of a femtosecond pulse is directly observable while the temporal amplitude is not. The frequency representation allowed us to include automatically dispersive broadening of both fundamental and SH pulses as well as their group mismatch, frequency dependence of the nonlinear susceptibility, frequency-dependent spatial profiles of the beams, and the blue shift of the SH spectrum (analog of self-steepening in fibers [50]). Furthermore, we have made a single approximation given by (15), which is easily avoidable in computer simulations. Equation (20) can also be used to describe the process of SH generation in the low pump-depletion regime to optimize a compressor needed to compensate phase distortions in the SH pulse. Extension of the theory to high conversion efficiency by including the second equation for the fundamental beam is also straightforward. Note that a similar frequency-domain approach to ultrashort-pulse propagation in optical fibers [62] helped solve a long-standing question of the magnitude of the shock term [50], [63].

V. ULTIMATE TEMPORAL RESOLUTION OF THE SHG FROG

In the general case of arbitrary pulses, the complete expression for the SHG FROG signal given by (27) must be computed numerically. However, for the limited class of pulses, such as linearly chirped Gaussian pulses, (27) can be evaluated analytically. Such analysis is valuable to estimate the temporal resolution of the SHG FROG experiment.

The geometrical smearing of the delay due to the crossing angle is an important experimental issue of the noncollinear multishot FROG measurement of ultrashort pulses. As can be seen from (27), the dependence on the transverse coordinate x yields a range of delays across the beam simultaneously which "blurs" the fixed delay between the pulses and broadens the FROG trace along the delay axis. Analogously to Taft et al. [9], we assume Gaussian-intensity pulses and, under perfect phase-matching conditions, obtain the measured pulse duration τ_{meas} that corresponds to a longer pulse as given by

$$
\tau_{\mathrm{meas}}^2 = \tau_p^2 + \delta t^2
\tag{28}
$$

where τ_p is the true pulse duration and δt is the effective delay smearing

$$
\delta t = \alpha_0 d_f / c
\tag{29}
$$

with d_f being the beam diameter in the focal plane and $2\alpha_0$ the intersection angle of the fundamental beams.

We consider the best scenario of the two Gaussian beams separated by their diameter d on the focusing optic. In this

case, the intersection angle $2\alpha_0 = d/f$ and the beam diameter in the focal plane $d_f = f\lambda/\pi d$, where f is the focal length of the focusing optic. Therefore, the resultant time smearing amounts only to $\delta t = \lambda/2\pi c \approx 0.4$ fs at $\lambda = 800$ nm. This value presents the ultimate resolution of the pulse measurement in the noncollinear geometry. Interestingly, this figure does not depend on the chosen focusing optic or the beam diameter d, since the beam waist is proportional whereas the intersection angle is inversely proportional to the focal distance f. It should be noted that the temporal resolution deteriorates if the beams are other than Gaussian. For instance, if the beams of the same diameter with a rectangular spatial intensity profile replace the Gaussian beams in the situation described above, the resultant temporal resolution becomes 0.7 fs.

Additional enhancement of the temporal resolution could be achieved either by placing a narrow slit behind the nonlinear medium [64], as will be discussed in Section X, or by employing a collinear geometry [65], [66].

VI. APPROXIMATE EXPRESSION FOR THE SHG FROG SIGNAL

In this section, our goal is to obtain a simplified expression for SHG FROG that can be used even for single-cycle optical pulses. We start from the complete expression given by (27) and show that the measured signal can be described by an ideal, i.e., perfectly phase-matched, SHG FROG and a spectral filter applied to the SH field. Throughout this section, we consider Type I phase matching.

In order to simplify (27), we make several approximations. First, as was shown in the previous section, under carefully chosen beam geometry the effect of geometrical smearing is negligibly small. For instance, it causes only a 10% error in the duration measurement of a 3-fs pulse and can be safely neglected. With such approximation, the integral along x in (27) can be performed analytically. Second, we assume that $\omega \approx \Omega/2$ and apply this to modify the factor that is proportional to the overlap area between different fundamental frequency modes: $\sqrt{\omega(1 - \omega/\Omega)} \approx \sqrt{\Omega}/2$. Third, we expand $k_O(\omega)$ and $k_O(\Omega - \omega)$ into Taylor series around $\omega = \Omega/2$ and keep the terms that are linear with frequency.[2] Hence, for Type I phase matching, we write

$$\Delta k(\omega, \Omega - \omega) \approx 2k_O(\Omega/2)\cos(\alpha_0 n_O(\Omega/2)) - k_E(\Omega)$$
$$= \Delta k(\Omega/2, \Omega/2). \tag{30}$$

Fourth, we estimate dispersion of the second-order susceptibility $\tilde{\chi}^{\langle 2 \rangle}(\Omega, \omega, \Omega - \omega)$ from the dispersion of the refractive index. For a classical anharmonic oscillator model [55], $\tilde{\chi}^{\langle 2 \rangle}(\Omega, \omega, \Omega - \omega) \propto \tilde{\chi}^{\langle 1 \rangle}(\Omega)\tilde{\chi}^{\langle 1 \rangle}(\omega)\tilde{\chi}^{\langle 1 \rangle}(\Omega - \omega)$, where $\tilde{\chi}^{\langle 1 \rangle}(\Omega) = n^2(\Omega) - 1$. Equation (27) can now be decomposed to a product of the spectral filter $R(\Omega)$, which originates from the finite conversion bandwidth of the SH crystal and varying
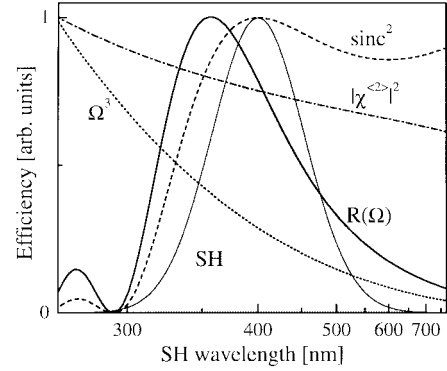

Fig. 3. Constituent terms of spectral filter $R(\Omega)$ given by (33). The Ω^3 dependence (dotted line), estimated squared magnitude of second-order susceptibility $\chi^{\langle 2 \rangle}$ (dash–dotted line), the crystal phase-matching curve for a Type I 10-μm BBO crystal cut at $\theta = 29°$ (dashed line), and their product (solid curve). The SH spectrum of a 3-fs Gaussian pulse is shown for comparison (shaded contour).

detector sensitivity, and an ideal FROG signal $S_{\text{FROG}}^{\text{SHG}}(\Omega, \tau)$

$$S(\Omega, \tau, L) \propto R(\Omega)S_{\text{FROG}}^{\text{SHG}}(\Omega, \tau) \tag{31}$$

where

$$S_{\text{FROG}}^{\text{SHG}}(\Omega, \tau) = \left| \int \tilde{\mathcal{E}}(\Omega - \omega)\tilde{\mathcal{E}}(\omega)\exp(i\omega\tau)\,d\omega \right|^2 \tag{32}$$

and

$$R(\Omega) = Q(\Omega)\frac{\Omega^3}{n_E(\Omega)}\left[\left(n_E^2(\Omega) - 1\right)\left(n_O^2(\Omega/2) - 1\right)^2\right]^2$$
$$\times \operatorname{sinc}^2\left(\frac{\Delta k(\Omega/2, \Omega/2)L}{2}\right). \tag{33}$$

In (31)–(33), we retained only the terms that are Ω-dependent.

The FROG signal given by (32) is the well-known classic definition of SHG FROG [14], [17], [34] written in the frequency domain. The same description is also employed in existing FROG retrieval algorithms. Note that the complete (27) can be readily implemented into the algorithm based on the method of generalized projections [67]. However, (31) is more advantageous numerically, since the integral (32) takes form of autoconvolution in the time domain and can be rapidly computed via fast Fourier transforms [68]. It is also important that the use of (31) permits a direct check of FROG marginals to validate experimental data.

The spectral filter $R(\Omega)$, as given by (33), is a product of several factors (see Fig. 3). The Ω^3-term (dotted line) results from the Ω dependence of the SH intensity on the spatial overlap of the different fundamental frequency modes,[3] and from the Ω^2 dependence that follows from Maxwell's equations. The meaning of the latter factor is that the generation of the higher frequency components is more efficient than of the lower frequency ones. The combined Ω^3 dependence leads to a substantial distortion of the SH spectrum of ultrabroad-band pulses. For instance, due to this factor alone, the upconversion efficiency of a spectral component at 600 nm is 4.5 times higher than of a 1000-nm one.

---

[2] Alternatively, one can perform Taylor expansion around the central frequency of the fundamental pulse $\omega = \omega_0$ [21], [38], [42]. However, in this case, the first derivative terms do not cancel each other and must be retained. Our simulations also prove that the expansion around $\omega = \Omega/2$ provides a better approximation when broad-band pulses are concerned.

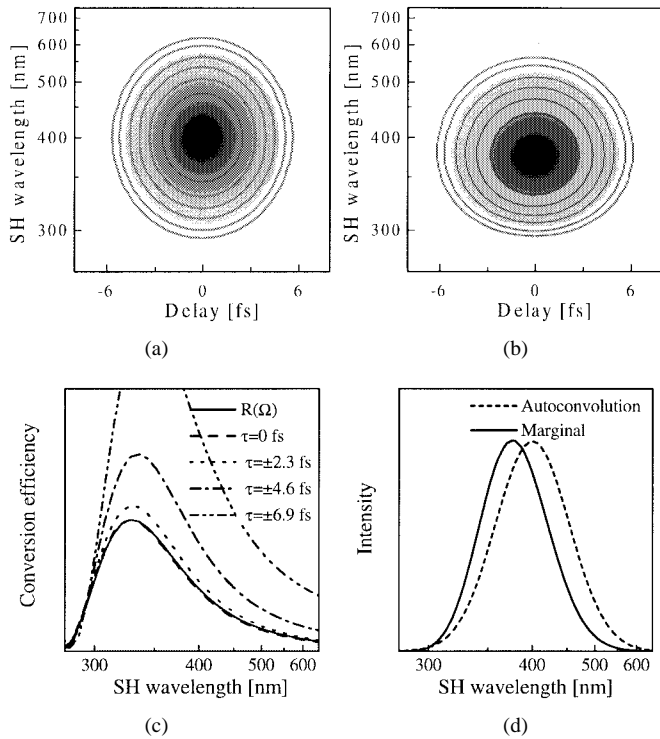[3] For a hollow fiber, this dependence should be disregarded [42], [53].

Fig. 4. Simulation of SHG FROG signal for an ideal 3-fs Gaussian pulse for Type I phase matching. (a) Ideal FROG trace as given by (32). (b) Complete FROG trace as given by (27). (c) Spectral filter curve $R(\Omega)$ computed according to (33) (shaded contour) and the ratio of FROG traces given in (b) and (a) at several delays (broken curves). (d) Spectral marginal of the traces shown in (b) (solid curve) and autoconvolution of the fundamental spectrum (dashed curve). The FROG traces here and further on are shown as density plots with overlaid contour lines at the values 0.01, 0.02, 0.05, 0.1, 0.2, 0.4, and 0.8 of the peak SH intensity.
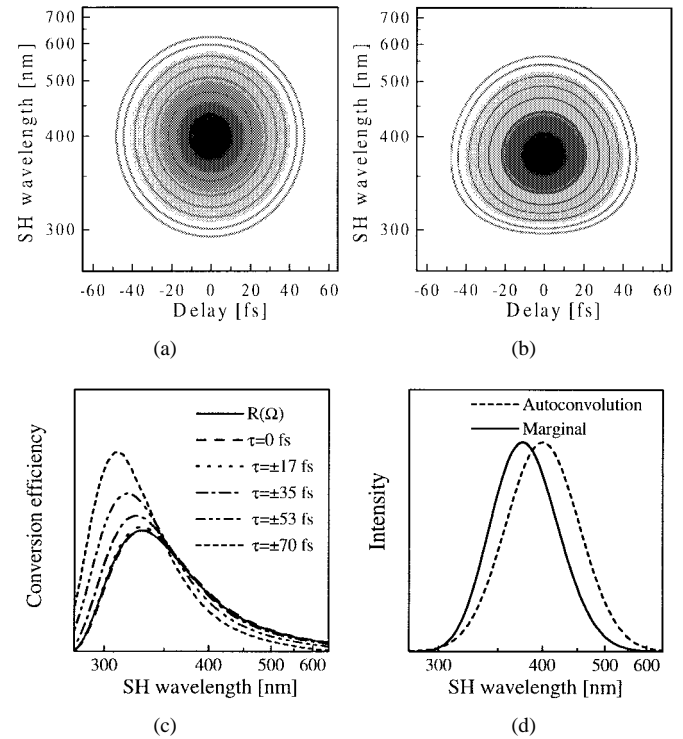
Fig. 5. Simulation of SHG FROG signal for a linearly chirped 26-fs Gaussian pulse. The conditions are the same as in Fig. 4. (a) Ideal FROG trace as given by (32). (b) Complete FROG trace as given by (27). (c) Spectral filter curve $R(\Omega)$ computed according to (33) (shaded contour) and the ratio of FROG traces given in (b) and (a) at several delays (broken curves). (d) Spectral marginal of the traces shown in (b) (solid curve) and autoconvolution of the fundamental spectrum (dashed curve).

The variation of the second-order susceptibility with frequency, expressed in (33) as the dependence on the refractive indices, plays a much less significant role than the Ω^3 factor (dotted line). According to our estimations for the BBO crystal, the squared magnitude of $\tilde{\chi}^{\langle 2 \rangle}$ for the 600-nm component of the fundamental wave is only 1.3 times larger than for the 1000-nm component. Such a virtually flat second-order response over the immense bandwidth is a good illustration of the almost instantaneous nature of $\tilde{\chi}^{\langle 2 \rangle}$ in transparent crystals. Nonetheless, estimation of the contribution of the $\tilde{\chi}^{\langle 2 \rangle}$ dispersion is required for the measurement of the optical pulses with the spectra that are hundreds of nanometers wide.

The last factor contributing to $R(\Omega)$ is the phase-matching curve of the SHG crystal (Fig. 3, dashed line). The shape and the bandwidth of this curve depend on the thickness, orientation and type of the crystal. Some practical comments on this issue will be provided in Section IX.

VII. NUMERICAL SIMULATIONS

In this section, we verify the approximations that were applied to derive (31)–(33). In order to do so, we numerically generate FROG traces of various pulses using the complete expression (27) and compare them with the ideal FROG traces calculated according to (32). To examine contributions of different factors to pulse reconstruction, we compare FROG inversion results with the input pulses.

Two types of pulses with the central wavelength at 800 nm are considered: 1) a bandwidth-limited 3-fs Gaussian pulse and 2) a pulse with the same bandwidth that is linearly chirped to 26 fs. We assume that the fundamental beam diameter in the focus is $d_f = 20$ μm and the beams intersect at $2\alpha_0 = 2°$. Therefore, the geometrical delay smearing that was defined in Section V [see (29)] amounts to $\delta t = 1.2$ fs. The $L = 10$ μm BBO Type I crystal is oriented for the peak conversion efficiency at 700 nm.[4] As we pointed out in Section IV, such a short crystal lengthens the pulse less than 0.1 fs, and, therefore, dispersive pulse broadening inside the crystal can be disregarded. The spectral sensitivity $Q(\Omega)$ of the light detector is set to unity.

The results of FROG simulations for each type of pulses are presented in Figs. 4 and 5. The ideal traces calculated according to (32) are shown in Figs. 4(a) and 5(a), while the traces computed using (27) are displayed in Figs. 4(b) and 5(b). The FROG trace of the 3-fs pulse is also noticeably extended along the delay axis as the consequence of the geometrical smearing. For the 26-fs pulse, as should be expected,

---

[4] The phase-matching angle is slightly affected by the noncollinear geometry. Due to the fact that the fundamental beams intersect at an angle $2\alpha_0$, the equivalent phase-matching angle is different from that in the case of collinear SHG: $\theta = \theta_{\text{collinear}} + \alpha_0/n$, where n is the refractive index of the fundamental wave at the phase-matching wavelength. For instance, the 800-nm phase-matched cut of a BBO crystal for $2\alpha_0 = 2°$ becomes $\theta = 29.6°$ instead of $\theta_{\text{collinear}} = 29°$ for collinear SHG. This fact should be kept in mind since the phase-matching curve is quite sensitive to the precise orientation of the crystal.
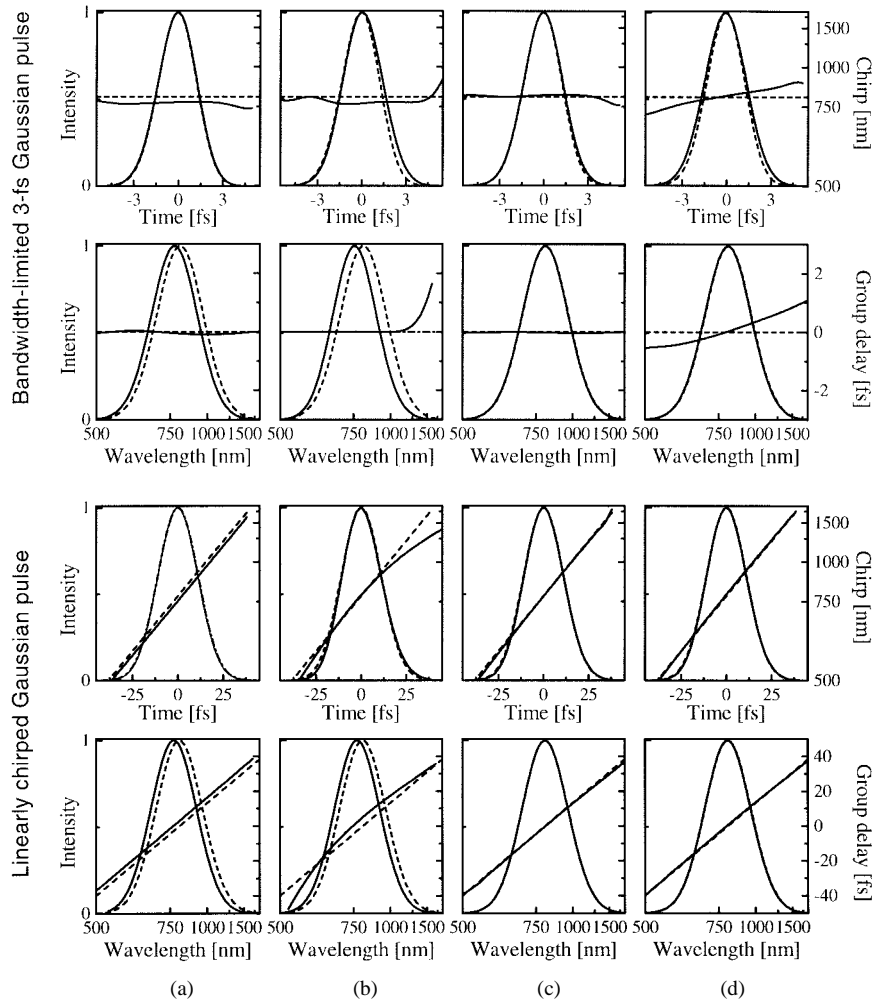
Fig. 6.   Retrieved pulse parameters in the time and frequency domains for various simulated FROG traces. (a) Perfectly phase-matched zero-thickness crystal, no geometrical smearing. (b) Type I 10-μm BBO crystal cut at $\theta = 33.4°$, no geometrical smearing. (c) The same as in (b), and the FROG trace is corrected according to (33). (d) The same as in (c) but with the geometrical smearing included. Dashed curves correspond to initial fields, while solid curves are obtained by FROG retrieval.

this effect is negligible. The spectral filtering occurring in the crystal becomes apparent from the comparison of the spectral marginals that are depicted in Figs. 4(d) and 5(d). Calculated marginals are asymmetric and substantially shifted toward shorter wavelengths.

By computing a ratio of the FROG signals given by (32) and (27), we obtain delay-dependent conversion efficiency, as shown in Figs. 4(c) and 5(c). The spectral filter $R(\Omega)$, calculated according to (33), is shown as shaded contours. Clearly, at the small delays τ, the conversion efficiency is almost exactly described by $R(\Omega)$. With the increase of pulse separation, the approximation given by (33) worsens, as both the conversion peak position and the magnitude change. The rapid ratio scaling at nonzero delays for the 3-fs pulse [broken curves in Fig. 4(c)] is mostly determined by the geometrical smearing rather than by the phase matching, as in the case of the chirped pulse [Fig. 5(c)]. On the other hand, the deviations from $R(\Omega)$ at longer delays become unimportant because of the decreasing signals at large pulse separations.

To estimate the significance of the spectral correction of the distorted FROG traces and feasibility of performing it in the case of extreme bandwidths, we examined FROG

inversion results of the numerically generated traces using the commercially available program from Femtosoft Technologies. Four different cases were considered for each type of pulses: 1) an ideal phase-matching (zero-thickness crystal); 2) a 10-μm BBO crystal with the parameters defined above; 3) the trace generated in case 2) is corrected by $R(\Omega)$; and 4) geometrical smearing is included as well. In its essence, case 4) is similar to 3), but in 4) the FROG trace was additionally distorted by the geometrical smearing. The results of the FROG inversion of cases 1)–(4) are presented in Fig. 6(a)–(d), respectively.

In Fig. 6(a), the Ω^3 dependence is exclusively responsible for the spectral filtering that substantially shifts the whole FROG trace along the frequency axis. Both the bandwidth-limited and the chirped Gaussian pulses showed excellent convergence to their input fields, but around a blue-shifted central frequency. In Fig. 6(b), where the phase-matching of a 10-μm BBO crystal is taken into account as well, the central wavelength is even more blue-shifted due to spectral filtering in the crystal. A small phase distortion is obtained for both types of pulses. The retrieved 3-fs pulse is also artificially lengthened to ~3.4 fs to match the bandwidth narrowed by the spectral filtering in the crystal. The results of FROG retrieval

of the same trace upon the correction by $R(\Omega)$ [Fig. 6(c)] indicate an excellent recovery of both the bandwidth-limited and the chirped pulses.

Finally, in Fig. 6(d) the geometrical smearing had a negligible effect on the 26-fs pulse. However, the FROG of the shorter pulse converged to a linearly chirped 3.3-fs Gaussian pulse. This should be expected, since the FROG trace broadens in time and remains Gaussian, while the spectral bandwidth is not affected. In principle, like the spectral correction $R(\Omega)$, the correction for the temporal smearing should also be feasible. It can be implemented directly into the FROG inversion algorithm by temporal averaging of the guess trace, produced in every iteration, prior to computing the FROG error.

Several important conclusions can be drawn from these simulations. First, they confirm the correctness of approximations used to obtain (31)–(33). Therefore, the spectral correction given by $R(\Omega)$ is satisfactory even in the case of single-cycle pulses, provided the crystal length and orientation permit one to maintain a certain, though not necessarily high, level of conversion over the entire bandwidth of the pulse. Second, a time-smearing effect does not greatly affect the retrieved pulses if the experimental geometry is carefully chosen. Third, the unmodified version of the FROG algorithm can be readily applied even to the shortest pulses. Fourth, it is often possible to closely reproduce the pulse parameters by FROG inversion of a spectrally filtered trace without any spectral correction [42]. However, such traces correspond to similar pulses shifted in frequency rather than to the original pulses for which they were obtained.

In order to quantify the distortions that are introduced into the SHG FROG traces by phase matching and the noncollinear geometry and that cannot be removed by the $R(\Omega)$-correction, we compute the systematic error as an rms average of the difference between the actual corrected FROG trace and the ideal trace normalized to unity. Given the form of the FROG error [18], the systematic error can be defined as follows:

$$G = \frac{1}{N}\sqrt{\sum_{i,j=1}^{N}\left| S_{\mathrm{FROG}}^{\mathrm{SHG}}(\Omega_i, \tau_j) - a\frac{S(\Omega_i, \tau_j, L)}{R(\Omega)}\right|^2} \quad (34)$$

where $S_{\mathrm{FROG}}^{\mathrm{SHG}}(\Omega, \tau)$ and $R(\Omega)$ are given by (32) and (33), respectively, and $S(\Omega, \tau, L)$ is computed according to (27). The parameter a is a scaling factor necessary to obtain the lowest value of G. The dependence of G on the duration of a bandwidth-limited pulse for the 128×128 FROG matrix that has optimal sampling along the time and frequency axes is presented in Fig. 7. As can be seen, the systematic error for $\sim$5-fs pulses becomes comparable with the typical achievable experimental SHG FROG error. It also should be noted that the contribution of geometrical smearing is about equal to or higher than that due to spectral distortions remaining after the spectral correction.

The systematic error should not be confused with the ultimate error achievable by the FROG inversion algorithm. Frequently, as, for instance, in the case of linearly chirped Gaussian pulses measured in the presence of geometrical smearing, it means that the FROG trace continues to exactly correspond to a pulse, but to a different one. However, for an
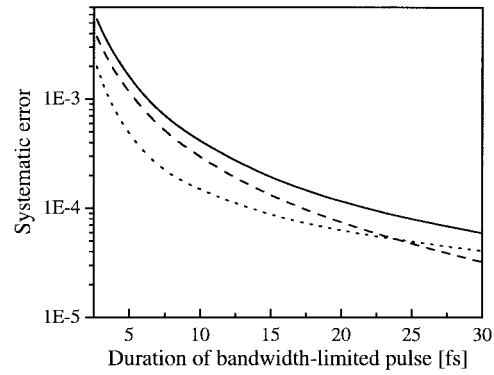

Fig. 7. Dependence of the systematic FROG trace error on the pulse duration. FROG matrix size is 128×128. The dotted curve corresponds to the trace after the spectral correction is given by (33). The error due to geometrical smearing of a perfectly phase-matched trace is shown as a dashed curve, while the error of a spectrally corrected and geometrically smeared FROG is given by the solid curve. The parameters of the crystal and of the geometrical smearing are the same as above. The central wavelength of the pulse is kept at 800 nm.

arbitrary pulse of $\sim$3 fs in duration, it is likely that the FROG retrieval error will increase due to the systematic error.

VIII. TYPE II PHASE MATCHING

So far, we have limited our consideration to Type I phase matching. In this section, we briefly discuss the application of Type II phase matching to the measurement of ultrashort laser pulses.

In Type II, the two fundamental waves are nonidentical, i.e., one ordinary and one extraordinary. This allows the implementation of the collinear SHG FROG geometry free of geometrical smearing [66]. The FROG traces generated in this arrangement in principle do not contain optical fringes associated with the interferometric collinear autocorrelation and, therefore, can be processed using the existing SHG FROG algorithms. However, the fact that the group velocities of the fundamental pulses in a Type II crystal become quite different has several important implications. First, the SH signal is no longer a symmetric function of the time delay [38]. Second, because the faster traveling fundamental pulse can catch up and pass the slower one, some broadening of the SH signal along the delay axis should be expected [38].

In order to check the applicability of the collinear Type II SHG FROG for the conditions comparable to those discussed earlier for the case of Type I phase matching, we performed numerical simulations identical to those in Section VII. The same pulses were used, i.e., the bandwidth-limited 3-fs pulse at 800 nm and the pulse with the same bandwidth stretched to 26 fs. The thickness of the Type II BBO is $L = 10\ \mu\mathrm{m}$, and the crystal is oriented for the peak conversion efficiency at 700 nm ($\theta = 45°$). The expression for the spectral filter, adapted for Type II, is given by

$$R(\Omega) = Q(\Omega)\frac{\Omega^3}{n_E(\Omega)}\left[\left(n_E^2(\Omega) - 1\right)\left(n_O^2(\Omega/2) - 1\right)\right.$$
$$\left. \times \left(n_E^2(\Omega/2) - 1\right)\right]^2 \mathrm{sinc}^2\left(\frac{\Delta k(\Omega/2, \Omega/2)L}{2}\right) \quad (35)$$
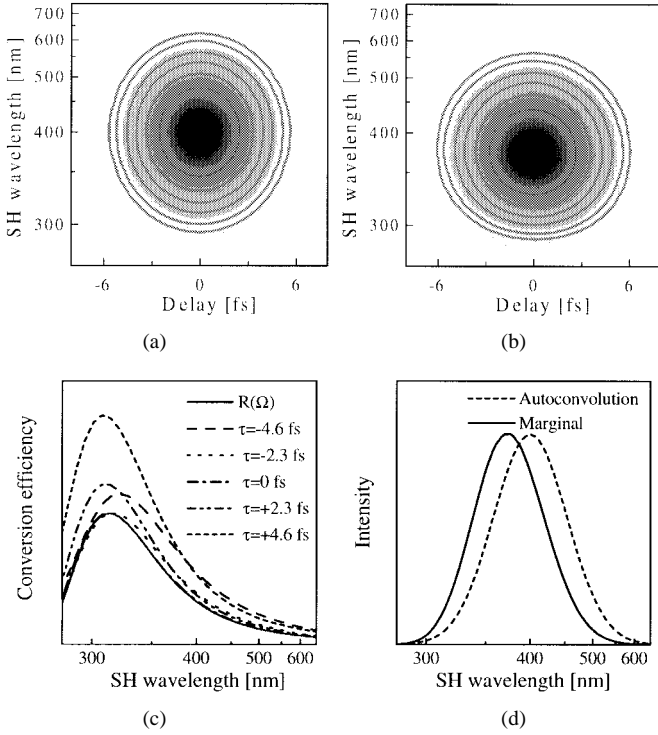
Fig. 8. Simulation of SHG FROG signal for an ideal 3-fs Gaussian pulse for Type II phase matching. (a) Ideal FROG trace as given by (32). (b) Complete FROG trace as given by (27). (c) Spectral filter curve $R(\Omega)$ computed according to (33) (shaded contour) and the ratio of FROG traces given in (b) and (a) at several delays (broken curves). (d) Spectral marginal of the traces shown in (b) (solid curve) and autoconvolution of the fundamental spectrum (dashed curve).
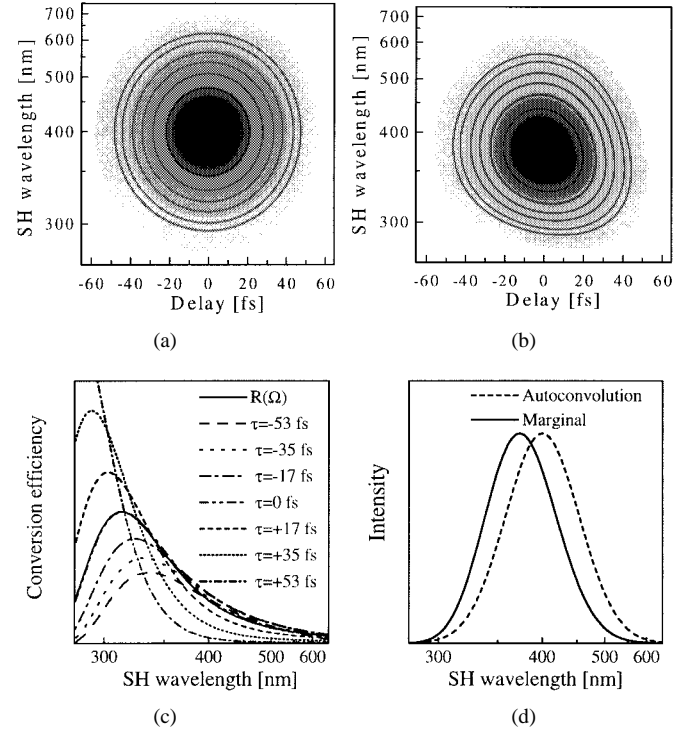
Fig. 9. Simulation of SHG FROG signal for a linearly chirped 26-fs Gaussian pulse. The conditions are the same as in Fig. 8. (a) Ideal FROG trace as given by (32). (b) Complete FROG trace as given by (27). (c) Spectral filter curve $R(\Omega)$ computed according to (33) (shaded contour) and the ratio of FROG traces given in (b) and (a) at several delays (broken curves). (d) Spectral marginal of the traces shown in (b) (solid curve) and autoconvolution of the fundamental spectrum (dashed curve). Note the skewness of the FROG trace in (b).

where the phase mismatch[5] is

$$\Delta k(\Omega/2, \Omega/2) = k_O(\Omega/2) + k_E(\Omega/2) - k_E(\Omega). \quad (36)$$

The results of FROG simulations are presented in Figs. 8 and 9. The FROG trace of the 3-fs pulse [see Fig. 8(b)] is practically symmetrical along the delay axis. However, despite the fact that no geometrical smearing has occurred, this trace is evidently broadened along the delay axis. Consequently, the FROG inversion of this trace after the spectral correction yields a longer $\sim$3.3-fs pulse. The elongation of the trace is due to the temporal walkoff of the fundamental waves, which in this case is about 1 fs. The magnitude of this temporal distortion is approximately equal to the geometrical smearing discussed in the previous section. The trace of the chirped pulse, produced under the same conditions [see Fig. 9(b)], is much more severely distorted than in the case of the bandwidth-limited pulse. The straightforward use of this trace is virtually impossible because of its strong asymmetry.

As in the Type I case, the conversion efficiency, obtained as a ratio of the ideal and simulated FROG traces, continues to correspond nicely to the spectral filter $R(\Omega)$ [see Figs. 8(c) and 9(c), shaded contours] at near-zero delays. Conversion efficiency at other delays, however, sharply depends on the sign of the delay τ. Similar to Type I phase matching, the frequency marginals [see Figs. 8(d) and 9(d)] are substantially

[5]Unlike the case of Type I phase matching, the first derivative terms do not cancel each other out, but they have been disregarded anyway.

blue-shifted. It is also apparent from Figs. 8(c) and 9(c) that the phase-matching bandwidth in this case is somewhat broader than in the analogous Type I crystal.

We can conclude from our simulations that Type II SHG FROG offers no enhancement of the temporal resolution and is less versatile compared to the noncollinear Type I arrangement. Additionally, the collinear Type II SHG FROG requires a greater experimental involvement than in the Type I SHG FROG. However, for some applications such as confocal microscopy, where the implementation of the noncollinear geometry is hardly possible due to the high numerical aperture of the focusing optics, the use of Type-II-based FROG appears quite promising [66].

IX. THE CHOICE OF THE SHG CRYSTAL

In this section, we provide several guidelines for selecting the correct SHG crystal in the FROG measurement. On the one hand, the crystal should be thick enough to generate an appropriate level of the SH signal for a high dynamic range measurement. One the other hand, the thickness of the crystal should be sufficiently small to provide an appropriate phase-matching bandwidth and minimize pulse broadening in the crystal.

Obviously, when choosing the crystal one must consider the bandwidth of the pulse that has to be characterized. We employ a simple criterion to estimate the required crystal thickness: the conversion efficiency calculated according to
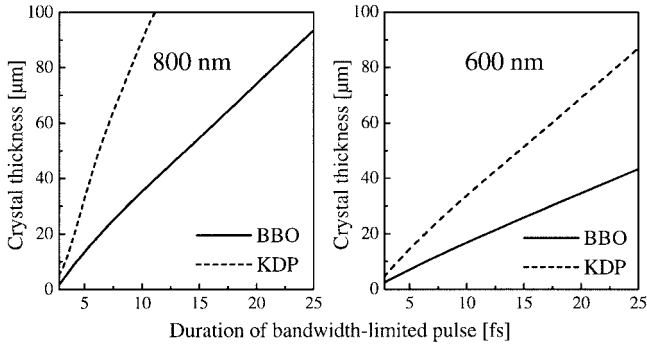
Fig. 10. Crystal thickness required for SHG FROG measurement as a function of the pulse duration at the central wavelength of (a) 800 nm and (b) 600 nm. The crystals are cut for Type I phase matching, which correspond to $\theta = 29°$ for BBO (solid line) and $\theta = 44°$ for KDP (dashed line).

(33) must be higher than 50% of the peak conversion efficiency everywhere over the double FWHM of the FROG spectral marginal. For the pulses that are Gaussian in frequency, the ideal spectral marginal, or the autoconvolution of the fundamental spectrum, is $\sqrt{2}$ times broader than the pulse bandwidth. Using this criterion, we evaluated BBO and KDP crystals, which are typically employed for ultrashort pulse measurement. Both considered crystals are cut for Type I phase matching at wavelengths of 800 and 600 nm. Fig. 10 depicts the appropriate crystal thickness of the BBO (solid curve) and KDP (dashed curve) as a function of duration of a bandwidth-limited Gaussian pulse.

As can be noted from Fig. 10, a BBO crystal approximately 10 μm-thick should be employed to measure 5-fs pulses at 800 nm. The adequate thickness of the KDP crystal is approximately 2.5 times larger due to its lower dispersion. However, while clearly providing an advantage in thickness, the KDP crystal has a disadvantage in the SHG efficiency. The signal level that can be obtained with a BBO crystal that is 2.5 times thinner is still approximately larger than in a KDP crystal by a factor of 6 because of the higher nonlinear coefficients and lower phase-matching angle in the BBO crystal [69]. Therefore, BBO is a more suitable choice for characterization of weak-intensity pulses. For high-intensity pulses, when the low level of the SH signal is not really the issue, KDP presents a better choice [42].

With the growth of the phase-matching bandwidth of the crystal, the Ω^3 dependence [see (33)] begins to dominate the conversion efficiency. As shown in Section VI, this dependence blue-shifts the SH spectrum. In case the phase-matching bandwidth of the SHG crystal is wider than required by the pulse bandwidth, angular tuning of the crystal can effectively counteract such blue-shift [42]. To illustrate the point, we consider a 10-μm BBO crystal applied to measure 8-fs Gaussian pulses at 800 nm. Fig. 11(a) shows the blue-shift of the FROG spectral marginal (filled circles) with respect to the autoconvolution (solid curve) if the crystal is perfectly phase-matched at 800 nm, i.e., $\theta = 29°$. However, after adjusting the phase-matching angle to $\theta = 24.4°$ that now corresponds to the central wavelength of 970 nm [see Fig. 11(b)], the phase-matching curve of the crystal (dashed curve) nearly perfectly balances the Ω^3 dependence (dotted
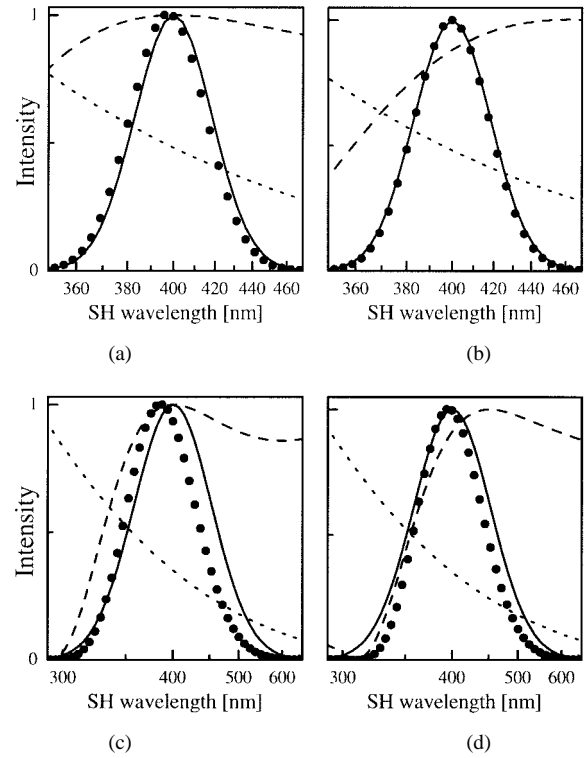

Fig. 11. Correction of frequency conversion efficiency by crystal orientation for (a), (b) 8-fs and (c), (d) 3-fs bandwidth-limited Gaussian pulses. A Type I 10-μm BBO crystal is oriented for the phase-matched wavelength of 800 nm (a), (c) and 970 nm (b), (d). The phase-matching curve and the Ω^3 dependence are shown as the dashed and dotted lines, respectively. The solid curves depict the autoconvolution of fundamental spectra, while spectral marginals of FROG traces are given by filled circles. In (b), no spectral correction of the FROG trace is required for an 8-fs pulse because of the red-shifted phase-matched wavelength. In contrast, the use of the 970-nm phase-matched crystal irreparably corrupts the SH spectrum in the case of a shorter 3-fs pulse (d). Note the difference in horizontal scales in (a), (b) and (c), (d).

curve). The overall conversion efficiency becomes almost flat and no spectral correction of the FROG trace is required. Experimentally, Taft et al. [9] demonstrated the effectiveness of the angular adjustment that enabled them to yield correct FROG data.

The mutual compensation of the Ω^3 and phase-matching terms is only possible for relatively long ($\sim$10-fs) pulses. As a thinner crystal is chosen to measure shorter pulses, the high-frequency slope of the phase-matching curve becomes relatively steeper than the low-frequency one [see Figs. 11(c) and (d)]. This is to be expected, since crystal dispersion is low in the infrared and increases approaching the ultraviolet (UV) absorption band. Tuning the central wavelength of the crystal from 800 nm [Fig. 11(c)] to 970 nm [Fig. 11(d)] substantially narrows the SH spectrum in the blue due to the crystal phase matching. Even worse, the FROG trace can hardly be corrected for the imposed spectral filter since the conversion efficiency becomes extremely low in the blue wing [Fig. 11(d)]. This should be contrasted to the 800-nm-cut case when the correction is still possible (see Fig. 6). Therefore, in order to extend the phase-matching bandwidth in the blue, one should consider using a crystal with the phase-matching wavelength blue-shifted with respect to the central frequency of the pulse. For example, a $L = 10$ μm BBO
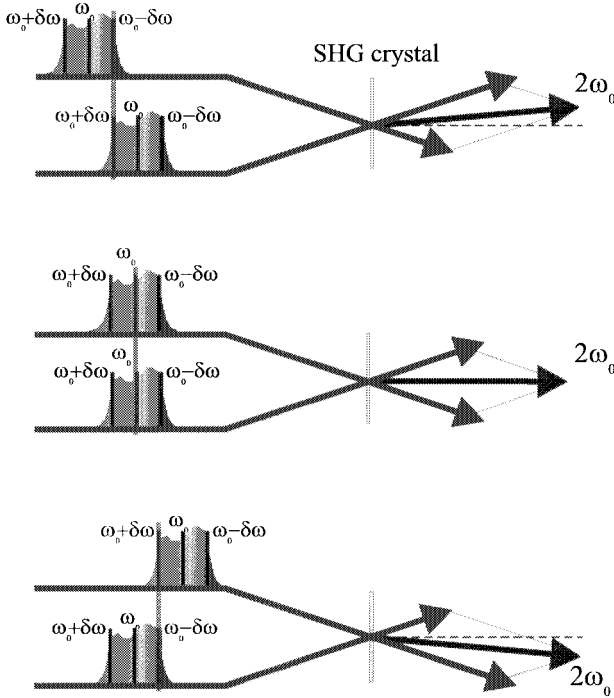
Fig. 12. Delay-dependent change of the SH direction in the case of a chirped pulse.
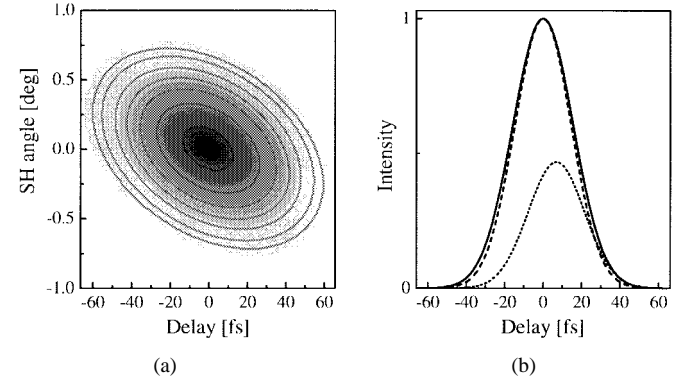

Fig. 13. Angular dependence of the noncollinear SH signal for a linearly chirped Gaussian pulse in the far field. (a) Autocorrelation intensity as a density plot of delay between the fundamental pulses and the SH angle. (b) Autocorrelation intensity trace obtained by integration over all spatial components of the SH beam (solid curve) and the traces detected through a narrow slit at the SH angle of $0°$ (dashed curve) and $0.4°$ (dotted curve). The pulse is stretched to ~5 times the bandwidth-limited pulse duration. The intersection angle of the fundamental beams is $2°$.

crystal oriented for peak conversion efficiency at 700 nm is more suitable for the measurement of sub-5-fs pulses centered at 800 nm than the same crystal tuned to 970 nm. Although the 700-nm-cut crystal has poorer conversion efficiency in the infrared, it nonetheless allows the extension of phase matching below 600 nm. Consequently, this crystal has an appreciable efficiency of frequency conversion all over the spectrum of a 5-fs pulse and, therefore, the FROG traces can be validated upon spectral correction. In contrast, information concerning the blue spectral wing is completely filtered out if the crystal oriented for 970 nm is used.

X. Spatial Filtering of the SH Beam

In this section, we show how spatial filtering of the SH beam can corrupt an autocorrelation or FROG trace. Unfortunately, this type of distortion can pass undetected since the FROG trace may still correspond to a valid pulse, but not the one that is being measured.

As already mentioned in Section IV [see (23)], the direction in which an SH frequency is emitted varies because of the noncollinear geometry. Even though the intersection angle of the fundamental beams is small, this effect becomes rather important for the measurement of broad-band pulses due to the substantial variation of the wavevector magnitude across the bandwidth.

Let us consider a certain component of the SH signal that has a frequency of $2\omega_0$ (Fig. 12). This component can be generated for several combinations of fundamental frequencies, for example, such as the pairs of ω_0 and ω_0, and of $\omega_0+\delta\omega$ and $\omega_0-\delta\omega$. The direction in which the $2\omega_0$ component is emitted

for each pair can vary, as determined by the noncollinear phase matching. Therefore, as can be seen from Fig. 12, the direction of the SH beam changes as a function of delay between the fundamental pulses. This phenomenon is utilized in the chirp measurement by angle-resolved autocorrelation [70], [71].

To illustrate the effect of spatial filtering of the SH beam, we examine the same Gaussian pulses linearly chirped to 26 fs, which were used in the numerical simulations described above. We keep the same geometrical parameters as in the previous sections of this paper, i.e., $d_f = 20$ μm and $2\alpha_0 = 2°$. The resulting dependence of the autocorrelation intensity as a function of the SH angle in the far field is depicted in Fig. 13(a). The tilt of the trace clearly indicates the sweep of the SH beam direction. The signal beam traverses approximately half the angle between the fundamental beams, and the magnitude of this sweep scales linearly with the intersection angle. The autocorrelation trace obtained by integration over all spatial components of the SH beam is depicted in Fig. 13(b) (solid curve). The FROG trace corresponding to this autocorrelation, i.e., measured by detecting of the whole beam, is entirely correct and allows recovery of the true pulse parameters.

The situation, however, becomes different if only a portion of the SH beam is selected. In the considered example, the autocorrelation or FROG, measured through a narrow slit placed on the axis of the second harmonic beam, would "shrink" along the delay axis, as shown in Fig. 13(b) (dashed curve). The width of this trace is $\sim10\%$ narrower than the true autocorrelation width. Positioning of the slit off the beam axis (see Fig. 13(b), dotted curve) leads to the shift of the whole trace along the delay axis and, for some pulses, to asymmetry in the autocorrelation wings. In the case of Gaussian pulses examined here, the FROG traces measured with such spatial selection remain self-consistent, disregarding the delay shift. The spectral marginal of such FROG traces is exactly the same as in the case of the whole-beam detection. Consequently, the FROG retrieval of the spatially filtered traces yields pulses of correct bandwidth but less chirped than in reality.
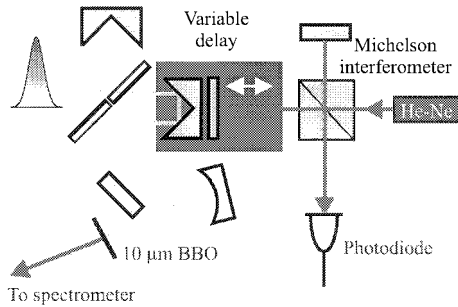
Fig. 14. Schematic of the SHG FROG apparatus. Spectrometer and its coupling optics are not shown.

The described effect should not be identified alone with the pulses that are much longer than the bandwidth limit, since even the bandwidth-limited pulses with asymmetric spectra carry a chirp in time. Therefore, careful collecting of all spatial components of the SH field is extremely essential. We also underline importance of measuring an independent autocorrelation trace in front of the spectrometer, since its comparison with the temporal marginal of the FROG trace might signal improper spatial filtration occurring in the FROG detection.

In Section V, we mentioned the ability to enhance the temporal resolution of a noncollinear measurement by placing a slit behind the nonlinear medium. This reduces the effective spot of the SH beyond the size of the diffraction-limited focus. However, placing a slit into the collimated beam would cause the spatial selection considered above. To avoid such undesirable distortion, one should position the slit behind the crystal within the Rayleigh range, or, alternatively, into the scaled image of the crystal plane projected by an achromatic objective lens. The realization of both these options is rather difficult and becomes really necessary only if the beams are poorly focusable.

XI. SHG FROG APPARATUS

In our experiments, we used pulses from a self-mode-locked cavity-dumped Ti:sapphire oscillator compressed upon chirping in a single-mode fused silica fiber. We measured the white-light continuum (WLC) pulses directly at the fiber output and, again, upon the their compression performed as described elsewhere [11].

The SHG FROG apparatus (Fig. 14) is based on a phase and amplitude balanced multishot autocorrelator designed for sub-5-fs short pulses [11]. The input beam was split and recombined in such a way that each of the beams travels once through an identical 50% beam splitter with both reflections occurring on the same coating–air interfaces.[6] To match the beam splitters, the initial horizontal polarization of the laser beam was rotated by a periscope. The moving arm of the autocorrelator was driven by a piezo transducer (Physik Instrumente) which is controlled by a computer via a digital–analog converter and a high-voltage amplifier. The precise time calibration was provided by an auxiliary Michelson interferometer.

[6]For shorter pulses, one should use lower reflectivity beam splitters that have a broader reflectivity range and flatter spectral phase.

The photodiode monitored the interference fringes that serve as time calibration marks.

Fundamental pulses were focused in the nonlinear crystal with an $r = -25$-cm spherical mirror at near normal incidence to minimize astigmatism. Due to the low curvature of the mirrors, delay variations within each beam are less than 0.1 fs. To achieve simultaneous upconversion of the entire fundamental bandwidth, we employed a 10-μm-thick BBO crystal cut for a central wavelength of 700 nm (EKSMA Inc.). Dispersive lengthening of a 5-fs pulse by such a crystal does not exceed 0.02 fs. The blue-shifted central wavelength permits one to extend the phase-matching bandwidth below 600 nm, as shown in Fig. 4(c). The cut angle of the crystal was verified with a tunable 100-fs laser. Retroreflection of the beams from the crystal surface provided exact reference for crystal orientation. This enables us to accurately calculate $R(\Omega)$ required for data correction according to (33). A visible-IR PC1000 (Ocean Optics) spectrometer was used to detect the fundamental spectra.

Two different SH detection systems were employed in the measurements of the compressed and the chirped pulses. In the case of compressed pulses, a well-characterized UV-Vis PC1000 (Ocean Optics) spectrometer was used. Therefore, the FROG traces could be readily corrected by $R(\Omega)$, as described above.

In the case of the strongly chirped pulses, a combination of a scanning monochromator and a photomultiplier tube provided the dynamic range necessary to measure the spectral wings (see Section XII). The reason for this was the following: the dynamic range of the measurement in a CCD-based spectrometer is determined not only by the spectral sensitivity, which is adequately high, but by the charge spreading all over the array due to the overload of some channels. To further extend the dynamic range, a lock-in amplifier was used to detect the SH signal. Because of the unknown spectral sensitivity $Q(\Omega)$, the spectral correction of the FROG traces in this case was performed according to the method suggested in Taft et al. [9], i.e., by using the ratio of the autoconvoluted fundamental spectrum and the spectral marginal.

XII. SHG FROG OF WHITE-LIGHT CONTINUUM

The study of the group delay of the chirped WLC is the corner stone of pulse compression. The phase measurement of the pulses leaving the fiber permits one to assess the feasibility of pulse compression in general. Understandably, the spectral phase must be sufficiently smooth to allow compensation by means of the existing dispersion control. A measurement of the spectral intensity, on the other hand, provides only a limited insight and reveals the minimum duration of the would-be compressed pulse. As an example of virtually uncompressible pulses, one might consider the case of spectral broadening due to a pure self-phase modulation. Furthermore, the task of building an appropriate pulse compressor is substantially eased if the phase distortion on the pulse is measured beforehand. This becomes increasingly important with the growth of the pulse spectral bandwidth that puts severe limitations on dispersion tunability of the pulse compressor. Therefore, it is desirable

to replace a great deal of "trial and error" work by measuring the phase distortion and computing the settings of the pulse compressor.

Somewhat counterintuitively, the FROG measurement of a strongly chirped pulse is considerably more complicated compared with the case a bandwidth-limited pulse with the identical spectrum.

First, the upconversion signals are weaker due to the lower peak power. This is evident, since the SH intensity of a pulse that is stretched to ten times its initial duration drops down 100 times.

Second, a higher dynamic range is required because of the uneven temporal spread of spectral wings. This occurs due to the high-order material dispersion. To explain this, we consider two spectral components with frequencies separated by 1000 cm^{-1}. The group delay accumulated between them after passing 1 mm of quartz amounts to 4 fs if these components are situated around 1000 nm and exceeds 11 fs in the case of 600 nm. Evaluating roughly, the corresponding elements of the FROG trace scale $\sim$7 times in intensity. In our experiments, the bandwidth of the WLC that needs to be captured in the FROG trace is broader than 10 000 cm^{-1}, and, therefore, the signal intensity varies very strongly across the resultant FROG traces.

The third complication is purely numerical, since FROG inversion demands greater matrix sizes to provide adequate sampling in both time and frequency domain. For the sake of speed, the FROG inversion algorithms employ fast Fourier transform (FFT) [68]. To avoid the loss of information in the change from the time domain to the frequency domain and vice versa, FFT requires equal number of points N in both these domains. Therefore, if the FROG matrix covers the total delay of $\Delta\tau N$ in the time domain, where $\Delta\tau$ is the time step, the spectral width represented in this trace is $N/\Delta\tau$. Compared with bandwidth-limited pulses, the pulses stretched in time require larger $\Delta\tau$ to contain the whole time information of the FROG trace in the matrix used in the FROG inversion algorithm. This narrows the spectral window covered by the matrix. Consequently, the number of points N (which in FFT is an integer power of two) must be increased to fully represent the FROG trace in the matrix used by the algorithm. This has an appreciable effect on the calculation speed. The change of N from 2^n to 2^{n+1}, where n is an integer, slows the FROG retrieval by a factor of $4(1 + n^{-1})$. In other words, by changing a 128×128 matrix with a 256×256 one increases the calculation time by a factor of $\sim$4.5.

Lastly, we point out the experimental inconvenience. In the case of strongly chirped pulses, the crystal alignment and the detected FROG trace become very sensitive to the delay-dependent change in the direction of the SH beam, as has already been discussed in Section X.

The SHG FROG traces of the chirped WLC in our experiments were recorded in 2.5-fs delay steps and converted into 256×256 matrices for processing. To reveal the conditions best suited for the compression of the WLC, we varied the parameters of the pulses entering the fiber by changing the settings of the prism precompressor. The intensity and chirp of the input pulses, derived by SHG FROG, are shown in Fig. 15(a). The measured and retrieved FROG traces of the

WLC are depicted in Figs. 15(b) and (c), and the retrieved WLC spectra and the group delay are shown in Fig. 15(d). The combined action of self-phase modulation and dispersion leads to a nearly linear group delay over most of the spectrum (Fig. 15(d), solid curves). The departure of the overall group delay from a linear asymptotic can be partly explained by the bulk dispersion of the fiber, air, and the beamsplitters in the FROG apparatus. For instance, while the optimal fiber length was estimated to be 1 mm [10], we employed a 2-mm piece for the practical convenience and in order to clean the exiting mode structure.

The WLC spectrum changes dramatically with the change of the input pulses (Fig. 15(d), shaded contours). The widest and least modulated spectrum corresponds to the almost chirp-free input pulse (Fig. 15(d), the third from the top panel). Positive as well as negative chirping leads to a substantial narrowing of the WLC spectrum. In contrast, the overall behavior of the group delays, shown as solid lines in Fig. 15(d), remains virtually unaffected. This ensures efficient pulse compression under different experimental conditions.

Group delay measurements of the generated continuum served as a target function for the design of the three-stage high-throughput compressor, consisting of a quartz 45°-prism pair, broad-band chirped mirrors, and thin-film Gires–Tournois dielectric interferometers [11]. The spectral bandwidth of the compressor is 590–1100 nm and is limited by the reflectivity of the employed chirped mirrors [72]. The phase characteristics of the compressor have been analyzed using dispersive ray tracing and mapped onto the measured group delay of the continuum. Fig. 16 depicts the measured group delay for different pulses, entering the fiber (shown as broken curves) which are reproduced from Fig. 15(d) and the calculated group delay of the pulse compressor (solid line). As one can see, our design compensates for the group delay of the white light everywhere across the compressor bandwidth. The adjustment of the material of the prism pair allows final fine optimization of the compressor dispersion, as judged from the FROG trace of the compressed pulses.

XIII. SHG FROG OF COMPRESSED PULSES

The FROG traces of the compressed pulses were recorded by incrementing the time delay between the arms in steps of 0.5 fs. The acquired 2-D arrays of points were converted into a 128×128 FROG matrix. The experimental and retrieved FROG traces of compressed pulses are depicted in Fig. 17(a) and (b). The FROG error amounted to 0.004 and is mainly caused by the noise in the spectral wings which scaled up after the spectral correction of the FROG trace. The temporal marginal of the FROG trace corresponds nicely with the independently measured intensity autocorrelation [see Fig. 17(a)] obtained by detecting the whole SH beam. This suggests that no spatial filtering of the SH beam has taken place. Comparison of the FROG frequency marginal and the autoconvolution of the fundamental spectrum [see Fig. 17(d)] indicates that no loss of spectral information has occurred.

Fig. 18 shows the retrieved intensity and phase in the time and frequency domains. To remove the time direction ambiguity in the measurement of the compressed pulses, we
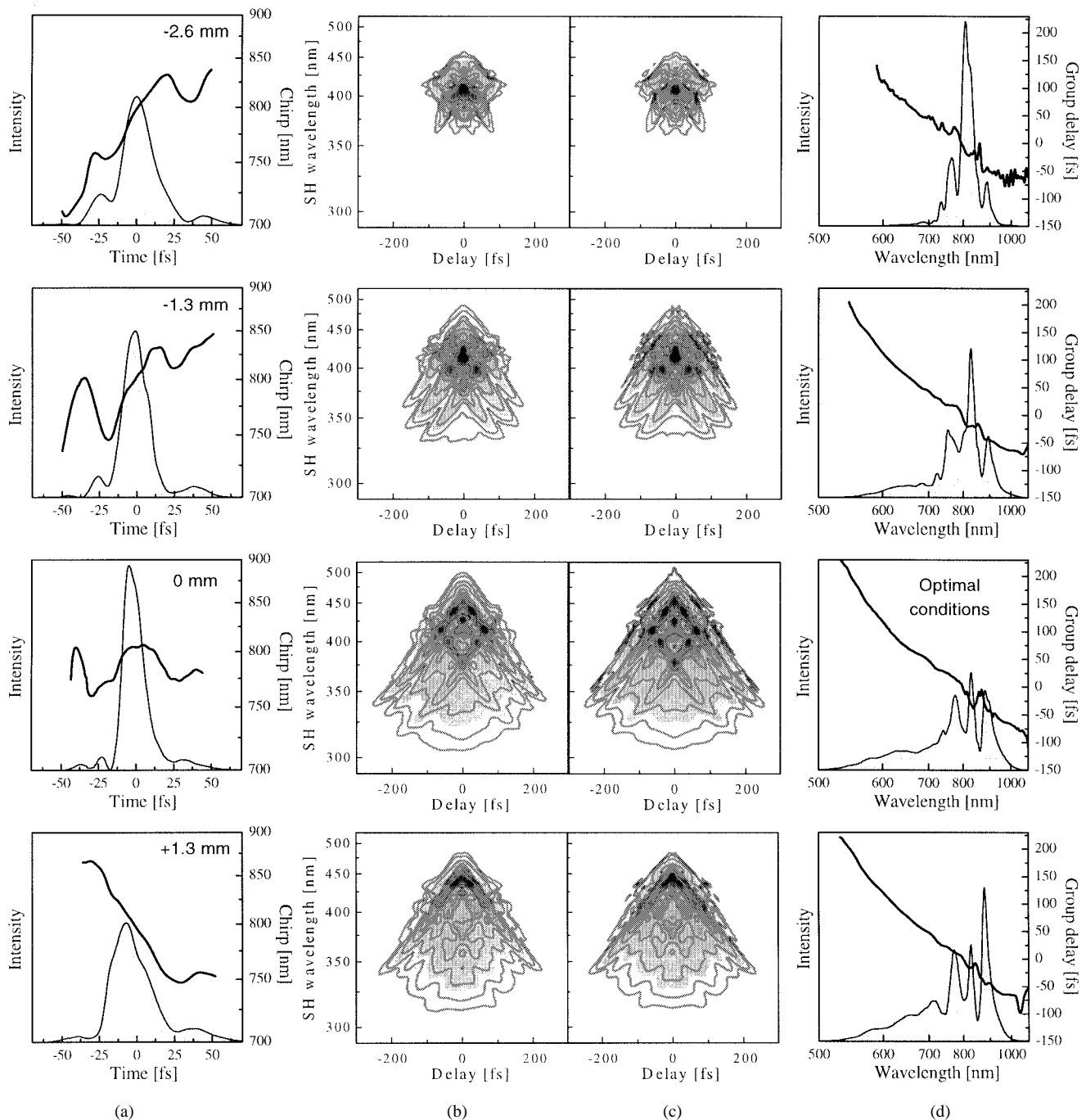
Fig. 15. Experimental results of FROG measurement of the strongly chirped WLC. (a) Temporal intensity (shaded contours) and chirp (solid curves) of the pulses entering a single-mode fused-silica fiber. (b) Measured and (c) retrieved SHG FROG traces of the WLC. (d) Retrieved spectral intensity (shaded contours) and the group delay of the WLC (solid curves). The amount of bulk material (fused silica) used to prechirp the input pulses is indicated in the right top corner of (a). Note that the input pulse energy is kept constant, while the respective scaling of the WLC spectra in (d) is preserved.

performed an additional FROG measurement introducing a known amount of dispersion (a thin fused silica plate) in front of the FROG apparatus. The obtained pulse duration is 4.5 fs while variations of the spectral phase [dashed line in Fig. 18(b)] is less than $\pm\pi/4$ across the whole bandwidth. These results fully confirm our previous analysis based on the interferometric autocorrelation [11].

To additionally verify both the self-consistency of our compressor calculations and the accuracy of the FROG retrieval, we compare the obtained spectral phase of the 4.5-fs pulse

(Fig. 18(b), dashed curve) with the predicted residual phase of the pulse compressor (Fig. 18(b), dash–dotted curve). The close similarity of the two reassures us of the correctness of all the procedures used, including the measurement of the chirped WLC, the knowledge of the dispersion of compressor constituent parts, the numerical routines employed for the ray tracing analysis, and, finally, the characterization of the compressed pulses.

The SHG FROG traces are generally considered unintuitive due to their symmetry along the delay axis [17], [19],
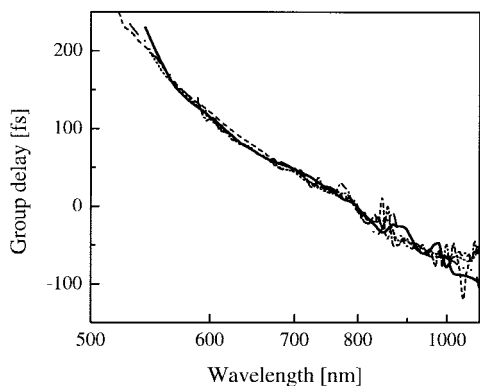
Fig. 16. Group delay of the designed pulse compressor. Solid curve is calculated by dispersive ray-tracing and is depicted reversed in time. The broken curves are the measured group delay of the WLC reproduced from all panels in Fig. 15(d).

Fig. 18. Retrieved parameters of 4.5-fs pulses in the (a) time and (b) frequency (b) domains. The FROG-retrieved intensity and phase are shown as shaded contours and dashed curves, respectively. Independently measured spectrum (filled circles) and computed residual phase of the pulse compressor (dash–dotted curve) are given in (b) for comparison.
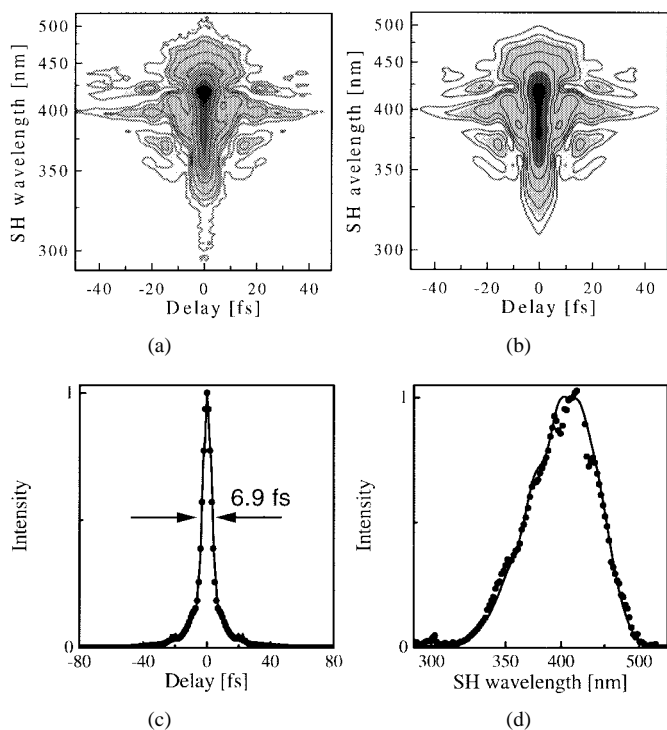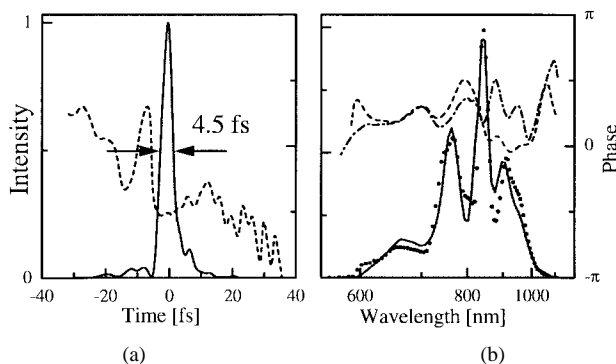

Fig. 17. The results of SHG FROG characterization of compressed pulses. (a) Experimental and (b) retrieved traces. (c) Temporal marginal (filled circles) and independently measured autocorrelation of 4.5-fs pulses (solid curve). (d) Frequency marginal (filled circles) and autoconvolution of the fundamental spectrum (solid curve).
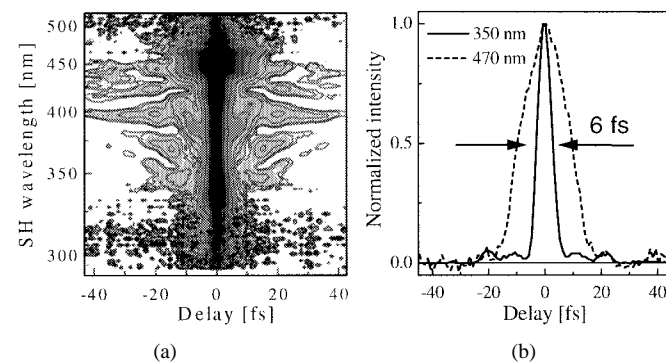

Fig. 19. Normalized FROG data of the 4.5-fs pulses. (a) SHG FROG trace of compressed pulses normalized along the delay axis as described in the text. (b) Autocorrelation traces derived from the FROG trace at the SH wavelength of 350 nm (solid curve) and 470 (dashed curve). Note that because of spectral selection the pulse duration estimated from the autocorrelation width can be both lower and higher than the real one and differ by as much as a factor of 3.

[34]. We found out that in the case of nearly bandwidth-limited pulses, one can significantly increase the amount of information available from the simple visual inspection of the trace. In order to do so, every trace in the time domain at its corresponding SH wavelength should be normalized to unity. Effectively, this represents the FROG trace as a series of normalized autocorrelations. In the case of the pulse with an arbitrary spectrum and the flat spectral phase, such representation of the SHG FROG trace would give a streak of uniform thickness around zero delay. The result of such operation applied to the FROG trace of the 4.5-fs pulse is

presented in Fig. 19(a). The variation of the thickness, i.e., the width of autocorrelation at a given SH wavelength, which can be seen in Fig. 19(a), indicates the nonperfect pulse compression without the necessity to run the FROG inversion algorithm.

Fig. 19(b) shows two autocorrelation traces derived from the spectrogram in Fig. 19(a) at two separate wavelengths. The FWHM of the autocorrelation at 350 nm is merely 6 fs, which is indicative of an ~4-fs pulse duration. However, the autocorrelation at 470 nm is three times broader. Such a difference clearly illustrates the effect of the spectral filtering in the nonlinear crystal as well as SH detection on the autocorrelation width. This also underscores the importance of pulse characterization by frequency-resolved (e.g., FROG) rather than nonfrequency-resolved (e.g., intensity autocorrelation) methods if one deals with such broad-band pulses.

Finally, we note that the width of the autocorrelation traces, such as the ones shown in Fig. 19(a), can be directly related to the instrument response of a spectroscopic experiment. For instance, the temporal resolution of a kinetic trace in a frequency-resolved pump-probe experiment [73], [74] detected at 950 nm will be ~12 fs, albeit the weighted average pulse

duration is 4.5 fs [75], [76]. Therefore, the frequency-resolved measurement (as FROG) brings invaluable information even if the correct estimation of the pulsewidth could be achieved by other simpler means, such as the autocorrelation measurement.

XIV. Conclusions and the Outlook

SHG FROG is a powerful and accurate pulse diagnostics technique that is ideally suited for the measurement of a vast variety of pulses. In particular, the instantaneous nonlinearity, high sensitivity, and broad-band response allow one to measure the shortest pulses available to date. The FROG measurement of the pulses that are shorter than 5 fs is nowadays probably the only available means to evaluate the pulse parameters and the temporal resolution of a nonlinear spectroscopic experiment.

In this paper, we have developed the SHG FROG description that includes phase matching in the SHG crystal, noncollinear beam geometry, and dispersion of the second-order nonlinearity. The derived master equation is valid down to single-cycle pulses. Furthermore, the numerical simulations have shown that the conventional description of FROG in the case of Type I phase matching can be readily used even for the single-cycle regime upon spectral correction of the FROG traces, provided the beam geometry, the finite crystal thickness, and phase-matching bandwidth are chosen correctly.

We have applied the developed theory to the SHG FROG measurement of 2.5-optical-cycle pulses with a central wavelength around 800 nm. To the best of our knowledge, these are the shortest pulses that have been completely characterized to date. We have also successfully measured strongly chirped weak-intensity pulses generated at the fiber output. These two key experiments that are required to design, test, and optimize the pulse compressor have both been performed without a single change in the SHG FROG apparatus. Under given conditions, no other pulse-measuring technique allows similar versatility.

FROG characterization of chirped spectrally broadened pulses offers an important shortcut in the generation of the ever-shorter pulses via external compression. The direct phase measurement of the output of glass fibers, as demonstrated in this paper, hollow waveguides [77], and parametric amplification [32], [78], [79] provides a rigorous target function for the pulse compressor design. In particular, we foresee clear benefits for two direct methods of pulse compression: adaptive dispersion control and all-mirror compression.

In the first case, the whole pulse compressor or one stage of it consists of the computer-controlled intensity and phase masks [80] or an acoustooptical modulator [81]. The required phase pattern can be calculated and set to match the target function measured by FROG. Such straightforward finding of the optimal conditions eliminates the time-consuming iterative search based on feedback [82] and guarantees a suitable phase correction.

In the second case, in which no flexible control over the resulting dispersion of the pulse compressor is permitted, the precise knowledge of the target function is even more important. The well-developed theory of chirped mirrors [83]

makes it possible to design the adequate dielectric layer structure that in many cases almost perfectly follows the required dispersion curve, measured by FROG. In general, the phase distortion of nearly any complexity can be compensated for by a mirror that is based on the gradient change of the refractive index instead of the discrete dielectric layers, as is the case with currently available chirped mirrors [72]. No doubt that with the growing interest in the intracavity [84], [85] and extracavity broad-band dispersion control [11], [32], [78], [86], the possibility of manufacturing the gradient-index structures will shortly become available. Therefore, the phase measurement of chirped pulses gains paramount importance.

References

[1] J. Zhou, J. Peatross, M. M. Murnane, H. C. Kapteyn, and I. P. Christov, "Enhanced high-harmonic generation using 25 fs laser pulses," *Phys. Rev. Lett.*, vol. 76, no. 5, pp. 752–755, 1996.

[2] C. J. Bardeen, Q. Wang, and C. V. Shank, "Selective excitation of vibrational wavepacket motion using chirped pulses," *Phys. Rev. Lett.*, vol. 75, no. 19, pp. 3410–3413, 1995.

[3] B. Kohler, V. V. Yakovlev, J. Che, J. L. Krause, M. Messina, K. R. Wilson, N. Schwentner, R. M. Whitnell, and Y. Yan, "Quantum control of wave packet evolution with tailored femtosecond pulses," *Phys. Rev. Lett.*, vol. 74, no. 17, pp. 3360–3363, 1995.

[4] V. V. Yakovlev, C. J. Bardeen, J. Che, J. Cao, and K. R. Wilson, "Chirped pulse enhancement of multiphoton absorption in molecular iodine," *J. Chem. Phys.*, vol. 108, no. 6, pp. 2309–2313, 1998.

[5] M. Fetterman, D. Goswami, D. Keusters, J.-K. Rhee, X.-J. Zhang, and W. S. Warren, "Generation of amplified shaped pulses for highly adiabatic excitation," in *Ultrafast Phenomena XI*, T. Elsaesser, J. G. Fujimoto, D. A. Wiersma, and W. Zinth, Eds. Berlin, Germany: Springer-Verlag, 1998, pp. 24–26.

[6] C. J. Bardeen, J. Che, K. R. Wilson, V. V. Yakovlev, P. Cong, B. Kohler, J. L. Krause, and M. Messina, "Quantum control of NaI photodissociation reaction product states by ultrafast tailored light pulses," *J. Phys. Chem.*, vol. 101, no. 20, pp. 3815–3822, 1997.

[7] A. Assion, T. Baumert, M. Bergt, T. Brixner, B. Keifer, V. Seyfried, M. Strehle, and G. Gerber, "Automated coherent control of chemical reactions and pulse compression by an evolutionary algorithm with feedback," in *Ultrafast Phenomena XI*, T. Elsaesser, J. G. Fujimoto, D. A. Wiersma, and W. Zinth, Eds. Berlin, Germany: Springer-Verlag, 1998, pp. 471–473.

[8] G. Taft, A. Rundquist, M. M. Murnane, and H. C. Kapteyn, "Ultrashort optical waveform measurement using frequency-resolved optical gating," *Opt. Lett.*, vol. 20, no. 7, pp. 743–745, 1995.

[9] G. Taft, A. Rundquist, M. M. Murnane, I. P. Christov, H. C. Kapteyn, K. W. DeLong, D. N. Fittinghoff, M. A. Krumbügel, J. Sweetser, and R. Trebino, "Measurement of 10-fs pulses," *IEEE J. Select. Topics Quantum Electron.*, vol. 2, pp. 575–585, May 1996.

[10] A. Baltuška, Z. Wei, M. S. Pshenichnikov, and D. A. Wiersma, "Optical pulse compression to 5 fs at a 1-MHz repetition rate," *Opt. Lett.*, vol. 22, no. 2, pp. 102–104, 1997.

[11] A. Baltuška, Z. Wei, M. S. Pshenichnikov, D. A. Wiersma, and R. Szipőcs, "All-solid-state cavity-dumped sub-5-fs laser," *Appl. Phys. B*, vol. 65, no. 2, pp. 175–188, 1997.

[12] M. Nisoli, S. D. Silvestri, R. Szipőcs, K. Ferencz, C. Spielmann, S. Sartania, and F. Krausz, "Compression of high-energy laser pulses below 5 fs," *Opt. Lett.*, vol. 22, no. 8, pp. 522–524, 1997.

[13] M. Nisoli, S. Stagira, S. D. Silvestri, O. Svelto, S. Sartania, Z. Cheng, M. Lenzner, C. Spielmann, and F. Krausz, "A novel-high energy pulse

compression system: Generation of multigigawatt sub-5-fs pulses," *Appl. Phys. B*, vol. 65, no. pp. 189–196, 1997.

[14] D. J. Kane and R. Trebino, "Characterization of arbitrary femtosecond pulses using frequency-resolved optical gating," *IEEE J. Quantum Electron.*, vol. 29, pp. 571–579, Feb. 1993.

[15] R. Trebino and D. J. Kane, "Using phase-retrieval to measure the intensity and phase of ultrashort pulses:frequency-resolved optical gating," *J. Opt. Soc. Amer.*, vol. 10, no. 5, pp. 1101–1111, 1993.

[16] D. N. Fittinghoff, K. W. DeLong, R. Trebino, and C. L. Ladera, "Noise sensitivity in frequency-resolved optical-gating measurements of utrashort pulses," *J. Opt. Soc. Amer. B*, vol. 12, no. 10, pp. 1955–1967, 1995.

[17] K. W. DeLong, R. Trebino, and D. J. Kane, "Comparison of ultrashort-pulse fequency-resolved-optical-gating traces for three common beam geometries," *J. Opt. Soc. Amer. B*, vol. 11, no. 9, pp. 1595–1608, 1994.

[18] K. W. DeLong, D. N. Fittinghoff, and R. Trebino, "Practical issues in ultrashort-laser-pulse measurement using frequency-resolved optical gating," *IEEE J. Quantum Electron*, vol. 32, pp. 1253–1264, July 1996.

[19] R. Trebino, K. W. DeLong, D. N. Fittinghoff, J. Sweetser, M. A. Krumbügel, B. Richman, and D. J. Kane, "Measuring ultrashort laser pulses in the time-frequency domain using frequency-resolved optical gating," *Rev. Sci. Instrum.*, vol. 68, no. 9, pp. 3277–3295, 1997.

[20] J.-K. Rhee, T. S. Sosnowski, A.-C. Tien, and T. B. Norris, "Real-time dispersion analyzer of femtosecond laser pulses with use of a spectrally and temporally resolved upconversion technique," *J. Opt. Soc. Amer.*, vol. 13, no. 8, pp. 1780–1785, 1996.

[21] J.-P. Foing, J.-P. Likforman, M. Joffre, and A. Migus, "Femtosecond pulse phase measurement by spectrally resolved up-conversion: Application to continuum compression," *IEEE J. Quantum. Electron.*, vol. 28, pp. 2285–2290, Oct. 1992.

[22] C. Iaconis and I. A. Walmsley, "Spectral phase interferometry for direct electric-field reconstruction of ultrashort optical pulses," *Opt. Lett.*, vol. 23, no. 10, pp. 792–794, 1998.

[23] I. A. Walmsley and V. Wong, "Characterization of the electric field of ultrashort optical pulses," *J. Opt. Soc. Amer.*, vol. 13, no. 11, pp. 2453–2463, 1996.

[24] V. Wong and I. A. Walmsley, "Ultrashort-pulse characterization from dynamic spectrograms by iterative phase retrieval," *J. Opt. Soc. Amer.*, vol. 14, no. 4, pp. 944–949, 1997.

[25] M. S. Pshenichnikov, K. Duppen, and D. A. Wiersma, "Time-resolved femtosecond photon echo probes bimodal solvent dynamics," *Phys. Rev. Lett.*, vol. 74, no. 5, pp. 674–677, 1995.

[26] P. Vöhringer, D. C. Arnett, T.-S. Yang, and N. F. Scherer, "Time-gated photon echo spectroscopy in liquids," *Chem. Phys. Lett.*, vol. 237, nos. 5–6, pp. 387–398, 1995.

[27] T. Steffen and K. Duppen, "Time resolved four- and six-wave mixing in liquids. II. Experiments," *J. Chem. Phys.*, vol. 106, no. 10, pp. 3854–3864, 1997.

[28] A. Tokmakoff and G. R. Fleming, "Two-dimensional Raman spectroscopy of the intermolecular modes of liquid CS2," *J. Chem. Phys.*, vol. 106, no. 7, pp. 2569–2582, 1997.

[29] A. Tokmakoff, M. J. Lang, D. S. Larsen, G. R. Fleming, V. Chernyak, and S. Mukamel, "Two-dimensional raman spectroscopy of vibrational interactions in liquids," *Phys. Rev. Lett.*, vol. 79, no. 14, pp. 2702–2705, 1997.

[30] K. Tominaga and K. Yoshihara, "Fifth order optical response of liquid CS2 observed by ultrafast nonresonant six-wave mixing," *Phys. Rev. Lett.*, vol. 74, no. 15, pp. 3061–3064, 1995.

[31] W. P. d. Boeij, M. S. Pshenichnikov, and D. A. Wiersma, "Ultrafast solvation dynamics explored by femtosecond photon echo spectroscopies," *Ann. Rev. Phys. Chem.*, pp. 99–123, 1998.

[32] A. Shirakawa, I. Sakane, and T. Kobayashi, "Sub-5-fs pulse generation by pulse-fron-matched optical parametric amplification," in *Ultrafast Phenomena XI*, T. Elsaesser, J. G. Fujimoto, D. A. Wiersma, and W. Zinth, Eds. Berlin, Germany: Springer-Verlag, 1998, pp. 54–56.

[33] K. W. DeLong, C. L. Ladera, R. Trebino, B. Kohler, and K. R. Wilson, "Ultrashort-pulse measurement using noninstantaneous nonlinearities: Raman effects in frequency-resolved optical gating," *Opt. Lett.*, vol. 20, no. 5, pp. 486–488, 1995.

[34] K. W. DeLong, R. Trebino, J. Hunter, and W. E. White, "Frequency-resolved optical gating with the use of second-harmonic generation," *J. Opt. Soc. Amer. B*, vol. 11, no. 11, pp. 2206–2215, 1994.

[35] J. Paye, M. Ramaswamy, J. G. Fujimoto, and E. P. Ippen, "Measurement of the amplitude and phase of ultrashort light pulses from spectrally resolved autocorrelation," *Opt. Lett.*, vol. 18, no. 22, pp. 1946–1948, 1993.

[36] J. Paye, "How to measure the amplitude and phase of an ultrashort light pulse with an autocorrelator and a spectrometer," *IEEE J. Quantum Electron.*, vol. 30, pp. 2693–2697, Nov. 1994.

[37] T. Tsang, M. A. Krumbügel, K. W. DeLong, D. N. Fittinghoff, and R. Trebino, "Frequency-resolved optical gating measurements of ultrashort pulses using surface third-harmonic generation," *Opt. Lett.*, vol. 21, no. 17, pp. 1381–1383, 1996.

[38] A. M. Weiner, "Effect of group velocity mismatch on the measurement of ultrashort optical pulses via second harmonic generation," *IEEE J. Quantum Electron.*, vol. QE-19, pp. 1276–1283, Aug. 1983.

[39] A. Baltuška, M. S. Pshenichnikov, and D. A. Wiersma, "Amplitude and phase characterization of 4.5-fs pulses by frequency-resolved optical gating," *Opt. Lett.*, vol. 23, no. 18, pp. 1474–1476, 1998.

[40] W. Rudolph and B. Wilhelmi, "Light pulse compression," *Laser Science and Technology*. Chur, Switzerland: Harwood, 1989.

[41] S. A. Akhmanov, V. A. Vysloukh, and A. S. Chirkin, *Optics of Femtosecond Laser Pulses*. New York: Amer. Inst. Phys., 1992.

[42] Z. Cheng, A. Fürbach, S. Sartania, M. Lenzner, C. Spielmann, and F. Krausz, "Amplitude and chirp characterization of high-power pulses in the 5-fs regime," *Opt. Lett.*, vol. 24, no. 4, 1999.

[43] C. Spielmann, N. H. Burnett, S. Sartania, R. Koppitsch, M. Shnürer, C. Kan, M. Lenzner, P. Wobrauschek, and F. Krausz, "Generation of coherent X-rays in the water window using 5-femtosecond laser pulses," *Science*, vol. 278, no. 5338, pp. 661–663, 1997.

[44] I. P. Christov, M. M. Murnane, and H. C. Kapteyn, "High-harmonic generation of attosecond pulses in the "Single-Cycle" Regime," *Phys. Rev. Lett.*, vol. 78, no. 7, pp. 1251–1254, 1997.

[45] L. Xu, C. Spielmann, A. Poppe, T. Brabec, F. Krausz, and T. W. Hänsch, "Route to phase control of ultrashort light pulses," *Opt. Lett.*, vol. 21, no. 24, pp. 2008–2010, 1996.

[46] L. V. Keldysh, "Ionization in the field of a strong electromagnetic wave," *Sov. Phys. JETF*, vol. 20, no. 5, pp. 1307–1314, 1965.

[47] I. P. Christov, "Propagation of femtosecond light pulses," *Opt. Commun.*, vol. 53, no. 6, pp. 364–366, 1984.

[48] P. U. Jepsen and S. R. Keiding, "Radiation patterns from lens-coupled terahertz antennas," *Opt. Lett.*, vol. 20, no. 8, pp. 807–809, 1995.

[49] S. Feng, H. G. Winful, and R. W. Hellwarth, "Gouy shift and temporal reshaping of focused single-cycle electromagnetic pulses," *Opt. Lett.*, vol. 23, no. 5, pp. 385–388, 1998.

[50] G. P. Agrawal, *Nonlinear Fiber Optics*, 2nd ed. San Diego, CA: Academic, 1995.

[51] D. Marcuse, "Gaussian approximation of the fundamental modes of graded-index fibers," *J. Opt. Soc. Amer.*, vol. 68, no. 1, pp. 103–109, 1978.

[52] E. A. J. Marcatili and R. A. Schmeltzer, "Hollow metallic and dielectric waveguides for long distance optical transmission and lasers," *Bell Syst. Tech. J.*, vol. 43, pp. 1783–1809, 1964.

[53] F. Krausz, private communication, 1998.

[54] H. Kogelnik and T. Li, "Beams, modes and resonators," in *Handbook of Lasers*, E. R. J. Pressley, Ed. New York: Chemical, 1971, pp. 421–441.

[55] R. W. Boyd, *Nonlinear Optics*. San Diego, CA: Academic, 1992.

[56] Y. R. Shen, *The Principles of Nonlinear Optics*. New York: Wiley, 1984.

[57] T. Brabec and F. Krausz, "Nonlinear optical pulse propagation in the single-cycle regime," *Phys. Rev. Lett.*, vol. 78, no. 17, pp. 3282–3285, 1997.

[58] N. Bloembergen, *Nonlinear Optics*. New York: Benjamin, 1965.

[59] Y. Wang and R. Dragila, "Efficient conversion of picosecond laser pulses into second-harmonic frequency using group-velocity dispersion," *Phys. Rev. A*, vol. 41A, no. 10, pp. 5645–5649, 1990.

[60] A. Umbrasas, J.-C. Diels, J. Jacob, G. Valiulis, and A. Piskarskas, "Generation of femtosecond pulses through second-harmonic compression of the output of a Nd:YAG laser," *Opt. Lett.*, vol. 20, no. 21, pp. 2228–2230, 1995.

[61] A. M. Weiner, A. M. Kan'an, and D. E. Leaird, "High-efficiency blue generation by frequency doubling of femtosecond pulses in a thick nonlinear crystal," *Opt. Lett.*, vol. 23, no. 18, pp. 1441–1443, 1998.

[62] P. V. Mamyshev and S. V. Chernikov, "Ultrashort-pulse propagation in optical fibers," *Opt. Lett.*, vol. 15, no. 19, pp. 1076–1078, 1990.

[63] J. T. Manassah, M. A. Mustafa, R. R. Alfano, and P. P. Ho, "Spectral extent and pulse shape of the supercontinuum for ultrashort laser pulse," *IEEE J. Quantum Electron.*, vol. QE-22, pp. 197–204, Jan. 1986.

[64] R. Trebino, private communication, 1997.

[65] J. A. Squier, D. N. Fittinghoff, C. P. J. Barty, K. R. Wilson, M. Müller, and G. J. Brakenhoff, "Characterization of femtosecond pulses focussed with high numerical aperture optics using interferometric surface-third-harmonic generation," *Opt. Commun.*, vol. 147, pp. 153–156, 1998.

[66] D. N. Fittinghoff, J. A. Squier, C. P. J. Barty, J. Sweetser, R. Trebino, and M. Müller, "Collinear Type II second-harmonic-generation

frequency-resolved optical gating for use with high-numerical aperture objectives," *Opt. Lett.*, vol. 23, no. 13, pp. 1046–1048, 1998.

[67] K. W. DeLong, D. N. Fittinghoff, R. Trebino, B. Kohler, and K. Wilson, "Pulse retrieval in frequency-resolved optical gating based on the method of generalized projections," *Opt. Lett.*, vol. 19, no. 15, pp. 2152–2154, 1994.

[68] W. H. Press, S. A. Teukolsky, W. T. Vetterling, and B. P. Flannery, *Numerical Recipes in C*. New York: Cambridge Univ., 1996.

[69] V. G. Dmitriev, G. G. Gurzadyan, and D. N. Nikogosyan, *Handbook of Non-Linear Optical Crystals*. Berlin, Germany: Springer-Verlag, 1991.

[70] V. Kabelka and A. V. Masalov, "Angularly resolved autocorrelation for single-shot time-frequency imaging of ultrashort light pulse," *Opt. Commun.*, vol. 121, nos. 4–6, pp. 141–148, 1995.

[71] V. Kabelka and A. V. Masalov, "Time-frequency imaging of a single ultrashort light pulse from angularly resolved autocorrelation," *Opt. Lett.*, vol. 20, no. 11, pp. 1301–1303, 1995.

[72] E. J. Mayer, J. Möbius, A. Euteneuer, W. W. Rühle, and R. Szipöcs, "Ultrabroadband chirped mirrors for femtosecond lasers," *Opt. Lett.*, vol. 22, no. 8, pp. 528–530, 1997.

[73] C. Rullère (Ed.), *Femtosecond Laser Pulses*. Berlin, Germany: Springer-Verlag, 1998, p. 310.

[74] C. H. B. Cruz, R. L. Fork, W. H. Knox, and C. V. Shank, "Spectral hole burning in large molecules probed with 10 fs optical pulses," *Chem. Phys. Lett.*, vol. 132, nos. 4–5, pp. 341–344, 1986.

[75] A. Kummrow, M. F. Emde, A. Baltuška, D. A. Wiersma, and M. S. Pshenichnikov, "Hydrated electron dynamics at a five femtosecond time scale," *Zeit. Phys. Chem.*, to be published.

[76] M. F. Emde, A. Baltuška, A. Kummrow, M. S. Pshenichnikov, and D. A. Wiersma, "Hydrated electron dynamics on a 5-fs time scale," in *Ultrafast Phenomena XI*, T. Elsaesser, J. G. Fujimoto, D. A. Wiersma, and W. Zinth, Eds. Berlin, Germany: Springer-Verlag, 1998, pp. 586–588.

[77] M. Nisoli, S. D. Silvestri, and O. Svelto, "Generation of high energy 10 fs pulses by a new pulse compression technique," *Appl. Phys. Lett.*, vol. 68, no. 20, pp. 2793–2795, 1996.

[78] G. Cerullo, M. Nisoli, S. Stagira, and S. D. Silvestri, "Ultrafast optics—Sub-8-fs pulses from an ultrabroadband optical parametric amplifier in the visible," *Opt. Lett.*, vol. 23, no. 16, pp. 1283–1285, 1998.

[79] T. Wilhelm, J. Piel, and E. Riedle, "Sub-20-fs pulses tunable across the visible from a blue-pumped single-pass noncollinear parametric converter," *Opt. Lett.*, vol. 22, no. 19, pp. 1494–1496, 1997.

[80] A. M. Weiner and A. M. Kan'an, "Femtosecond pulse shaping for synthesis, processing, and time-to-space conversion of ultrafast optical waveforms," *IEEE J. Select. Topics Quantum Electron.*, vol. 4, pp. 317–331, Mar. 1998.

[81] C. W. Hillegas, J. X. Tull, D. Goswami, D. Strickland, and W. S. Warren, "Femtosecond laser pulse shaping by use of microsecond radio-frequency pulses," *Opt. Lett.*, vol. 19, no. 10, pp. 737–739, 1994.

[82] D. Yelin, D. Meshulach, and Y. Silberberg, "Adaptive femtosecond compression," *Opt. Lett.*, vol. 22, no. 23, pp. 1793–1795, 1997.

[83] R. Szipöcs and A. Köházi-Kis, "Theory and design of chirped dielectric mirrors," *Appl. Phys. B*, vol. 65, no. 2, pp. 115–136, 1997.

[84] L. Xu, C. Spielmann, F. Krausz, and R. Szipöcs, "Ultrabroadband ring oscillator for sub-10-fs pulse generation," *Opt. Lett.*, vol. 21, no. 16, pp. 1259–1261, 1996.

[85] I. D. Jung, F. X. Kärtner, N. Matuschek, D. H. Sutter, F. Morier-Genoud, G. Zhang, U. Keller, V. Scheuer, and M. Tilsch, "Self-starting 6.5-fs pulses from a Ti:sapphire laser," *Opt. Lett.*, vol. 22, no. 13, pp. 1009–1011, 1997.

[86] S. Sartania, Z. Cheng, M. Lenzner, G. Tempea, C. Spielmann, F. Krausz, and K. Ferencz, "Generation of 0.1-TW 5-fs optical pulses at a 1-kHz repetition rate," *Opt. Lett.*, vol. 22, no. 20, pp. 1562–1564, 1997.

Andrius Baltuška received the diploma in physics from Vilnius University, Lithuania, in 1993. He is currently working toward the Ph.D. degree in physics at the University of Groningen, Groningen, The Netherlands.

His research is focused on femtosecond nonlinear spectroscopy and on generation and characterization of ultrashort pulses.

Mr. Baltuška has held an Ubbo Emmius graduate fellowship founded by the University of Groningen since 1996.

Maxim S. Pshenichnikov received the Ph.D. degree in physics from Moscow State University (MSU), USSR, in 1987, in the field of quantum electronics.

He joined the faculty at MSU in 1986 and worked in the Department of Physics and International Laser Centre where he conducted experiments on four-wave mixing in alkaline metal vapor, optical phase-conjugation, IR image upconversion, and remote control of atmospheric pollutants. In 1992, he moved to the Ultrafast Lasers and Spectroscopy Laboratory at the University of Groningen, The Netherlands, where he assumed a Senior Research Associate position in 1996. His current research interests include ultrafast optical dynamics and charge-transfer reactions in liquid phase, interferometric effects in molecular media, and generation, amplification, and characterization of femtosecond pulses.

Dr. Pshenichnikov is a member of the Optical Society of America.
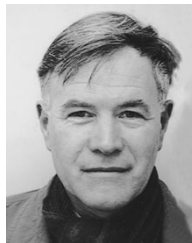
Douwe A. Wiersma received the Ph.D. degree from the University of Groningen, The Netherlands, in 1969.

From 1969 to 1971, he continued his studies as a Post-Doctoral Fellow in the group of Prof. Hochstrasser at the University of Pennsylvania, Philadelphia. On return to The Netherlands, he was appointed an Assistant Professor at the University of Groningen, promoted to Associate Professor in 1977, and became Full Professor of Physical Chemistry in 1981. In 1981–1982, he spent a sabbatical year with Prof. Fayer at Stanford University, Stanford, CA. His long-standing interests are in the field of photon echo phenomena, recently on a femtosecond time scale. Within this field, he has developed a variety of new techniques, some of which have been used worldwide to obtain a fundamental understanding of the condensed phase optical dynamics. Recently, these techniques were also been applied to biological systems.

Dr. Wiersma is a member of the Royal Dutch Academy of Sciences, a fellow of the American Physical Society, and a member of the Optical Society of America. In 1976, he was awarded the Royal Netherlands Chemistry Society Medal for his work on photon echoes in molecular solids. In 1998, he was awarded the 13th Physics-Lecture prize of the Dutch Physics Society.